

Data-driven model reduction via non-intrusive optimization of projection operators and reduced-order dynamics

Alberto Padovan*, Blaine Vollmer*, and Daniel J. Bodony*

Abstract. Computing reduced-order models using non-intrusive methods is particularly attractive for systems that are simulated using black-box solvers. However, obtaining accurate data-driven models can be challenging, especially if the underlying systems exhibit large-amplitude transient growth. Although these systems may evolve near a low-dimensional subspace that can be easily identified using standard techniques such as Proper Orthogonal Decomposition (POD), computing accurate models often requires projecting the state onto this subspace via a non-orthogonal projection. While appropriate oblique projection operators can be computed using intrusive techniques that leverage the form of the underlying governing equations, purely data-driven methods currently tend to achieve dimensionality reduction via orthogonal projections, and this can lead to models with poor predictive accuracy. In this paper, we address this issue by introducing a non-intrusive framework designed to simultaneously identify oblique projection operators and reduced-order dynamics. In particular, given training trajectories and assuming reduced-order dynamics of polynomial form, we fit a reduced-order model by solving an optimization problem over the product manifold of a Grassmann manifold, a Stiefel manifold, and several linear spaces (as many as the tensors that define the low-order dynamics). Furthermore, we show that the gradient of the cost function with respect to the optimization parameters can be conveniently written in closed form, so that there is no need for automatic differentiation. We compare our formulation with state-of-the-art methods on three examples: a three-dimensional system of ordinary differential equations, the complex Ginzburg-Landau (CGL) equation, and a two-dimensional lid-driven cavity flow at Reynolds number $Re = 8300$.

Key words. Model reduction, Data-driven reduced-order models, Manifold optimization, Operator inference.

AMS subject classifications. 37M05, 37M10, 37N10

1. Introduction. Computing reduced-order models (ROMs) of high-dimensional systems is often necessary to perform several tasks, including accelerating expensive simulations, developing control strategies and solving design optimization problems. Most model reduction frameworks share the following key ingredients: a possibly nonlinear map from the high-dimensional state space to a low-dimensional space (i.e., an encoder), a possibly nonlinear map from the low-dimensional space to the original high-dimensional space (i.e., a decoder), and reduced-order dynamics to evolve the reduced-order state. Here, we provide a brief review of intrusive and non-intrusive methods where the reduced-order dynamics are continuous in time, and where the encoder and decoder define linear projection operators (i.e., the encoder and decoder are linear maps and the encoder is a left-inverse of the decoder).

Perhaps the most well-known reduced-order models that fall within this category are the so-called linear-projection Petrov-Galerkin models. These are obtained by (obliquely) projecting the full-order dynamics onto a low-dimensional linear subspace. In particular, given a decoder $\Phi(\Psi^T\Phi)^{-1}$ and an encoder Ψ^T , where Φ and Ψ are tall rectangular matrices that define a projection $\mathbb{P} = \Phi(\Psi^T\Phi)^{-1}\Psi^T$, the aforementioned linear subspace is given by

*Department of Aerospace Engineering, University of Illinois at Urbana-Champaign, Urbana, IL, 61801 (padovan3@illinois.edu)

41 the span of Φ , and Ψ specifies the direction of projection. This is illustrated in figure 1 in [32].
 42 If $\Phi = \Psi$, then the projection \mathbb{P} is orthogonal and the model is known as a Galerkin model.
 43 In the simplest of cases, a Galerkin model can be obtained by orthogonally projecting the
 44 dynamics onto the span of the leading Proper Orthogonal Decomposition (POD) modes of
 45 a representative training data set. This procedure is “weakly” intrusive in the sense that it
 46 requires access to the governing equations, but not necessarily to the linearization and adjoint
 47 of the underlying nonlinear dynamics. In the context of fluids, POD-Galerkin models have
 48 been used extensively for both compressible and incompressible flows [31, 23, 2, 32]. However,
 49 these models may not perform well in systems that exhibit large-amplitude transient growth.
 50 Examples of such systems in fluid mechanics include boundary layers, mixing layers, jets and
 51 high-shear flows in general [8]. The difficulty posed by these systems can often be traced
 52 back to the non-normal¹ nature of the underlying linear dynamics, which demands the use of
 53 carefully chosen oblique projections. In linear systems, or nonlinear systems that evolve near
 54 a steady state, this problem can be addressed using methods such as Balanced Truncation [22,
 55 11, 39] or Balanced POD [30], which produce oblique projection operators and corresponding
 56 Petrov-Galerkin models by balancing the observability and reachability Gramians associated
 57 with the underlying linear dynamics. Extensions and variants of Balanced Truncation and
 58 Balanced POD also exist for quadratic-bilinear systems [4] and for systems that evolve in
 59 the proximity of time-periodic orbits [38, 20, 27]. Beyond balancing, we find several other
 60 approaches from linear systems theory, including \mathcal{H}_2 and \mathcal{H}_∞ model reduction, where reduced-
 61 order models are obtained by minimizing the \mathcal{H}_2 and \mathcal{H}_∞ norms of the error between the full-
 62 order and reduced-order transfer functions [37, 12]. As in the case of balancing, extensions of
 63 \mathcal{H}_2 -optimal (and quasi-optimal) model reduction were developed for quadratic-bilinear systems
 64 [3, 5]. For highly nonlinear systems that lie outside the region of applicability of linear
 65 model reduction methods, one can turn to recently-developed methods such as Trajectory-
 66 based Optimization of Oblique Projections (TrOOP) [25] and Covariance Balancing Reduction
 67 using Adjoint Snapshots (COBRAS) [26]. TrOOP identifies optimal oblique projections for
 68 Petrov-Galerkin modelling by training against trajectories generated by the full-order model,
 69 while COBRAS identifies oblique projections for model reduction by balancing the state and
 70 gradient covariances associated with the full-order solution map. We shall see that our non-
 71 intrusive formulation is closely related to TrOOP, so we will discuss the latter in more detail in
 72 section 2.5. All these Petrov-Galerkin methods are intrusive: not only do they require access
 73 to the full-order dynamics, but also to their linearization about steady or time-varying base
 74 flows and to the adjoint of the linearized dynamics. Thus, they are not easily applicable to
 75 systems that are simulated using black-box solvers.

76 Among existing techniques to obtain data-driven reduced-order models with continuous-
 77 time dynamics on linear subspaces, the most well-known is perhaps Operator Inference [28, 19].
 78 Operator Inference fits a model to data by minimizing the difference between (usually polyno-
 79 mial) reduced-order dynamics and the projection of the time-derivative of the full-order state
 80 onto a low-dimensional subspace. Usually, this subspace is defined by the span of POD modes,

¹A non-normal linear operator is one whose right eigenvectors are not mutually orthogonal, and, in the context of fluids, non-normality is due to the presence of the advective transport terms in the Navier-Stokes equation.

81 and the high-dimensional data are projected orthogonally onto it. While Operator Inference
 82 has been shown to work well for systems that evolve in close proximity of an attractor (see,
 83 e.g., [29]), it may suffer from the aforementioned drawbacks of orthogonal projections when
 84 applied to highly non-normal systems evolving far away from an attractor (e.g., during tran-
 85 sients). This will become apparent in the examples sections. In the interest of completeness,
 86 it is worth mentioning that the Operator Inference framework is not limited to linear spaces.
 87 In fact, Operator Inference reduced-order models were recently computed after orthogonally
 88 projecting the data onto quadratic manifolds [14, 6], and extensions of the Operator Infer-
 89 ence formulation were developed to preserve the underlying structure or symmetries of the
 90 full-order model [35, 15, 18]. We conclude our brief review by acknowledging that there exist
 91 several other non-intrusive model reduction frameworks in the literature (e.g., discrete-time
 92 formulations such as dynamic mode decomposition (DMD), autoencoders parameterized via
 93 neural networks, and many others), and we will mention those that are more closely connected
 94 with our formulation as needed throughout the manuscript.

95 In this paper, we introduce a novel non-intrusive framework to address the problems associ-
 96 ated with orthogonal projections. In particular, given training trajectories from the full-order
 97 model, we fit an optimal low-order model by simultaneously seeking reduced-order dynamics
 98 \mathbf{f}_r and oblique projection operators \mathbb{P} defined by a linear encoder Ψ^\top and a linear decoder
 99 $\Phi(\Psi^\top\Phi)^{-1}$. We shall see that the optimization parameters are the subspace $V = \text{Range}(\Phi)$,
 100 which lives naturally on the Grassmann manifold, the matrix Ψ , which can be taken to be an
 101 element of the orthogonal Stiefel manifold, and the parameters that define the reduced-order
 102 dynamics (e.g., reduced-order tensors if the dynamics are taken to be polynomial). Fur-
 103 thermore, if we constrain the reduced-order dynamics \mathbf{f}_r to be of a form that lends itself to
 104 straightforward differentiation (e.g., polynomial), we show that the gradient of the cost func-
 105 tion with respect to the optimization parameters can be written in closed form. This is quite
 106 convenient because it bypasses the need for automatic differentiation and it allows for faster
 107 training. We test our formulation on three different examples: a simple system governed by
 108 three ordinary differential equations, the complex Ginzburg-Landau (CGL) equation and the
 109 two-dimensional incompressible lid-driven cavity flow at Reynolds number $Re = 8300$. On all
 110 three examples, we compare our framework with Operator Inference and POD-Galerkin. In
 111 the first two examples, we also compare with TrOOP, which has been shown to give very accu-
 112 rate Petrov-Galerkin models in several examples, including highly non-normal and nonlinear
 113 jets [25, 26]. On all three examples, our models exhibit better performance than Operator
 114 Inference and POD-Galerkin models, and in the first two examples we obtain models with
 115 predictive accuracy very close to that of the intrusive TrOOP formulation.

116 **2. Mathematical formulation.** Throughout this section, we consider a general nonlinear
 117 system with dynamics defined by

$$118 \quad (2.1) \quad \begin{aligned} \frac{d\mathbf{x}}{dt} &= \mathbf{f}(\mathbf{x}, \mathbf{u}), & \mathbf{x}(0) &= \mathbf{x}_0 \\ \mathbf{y} &= \mathbf{h}(\mathbf{x}) \end{aligned}$$

119 where $\mathbf{x} \in \mathbb{R}^n$ is the state vector, \mathbf{x}_0 is the initial condition, $\mathbf{u} \in \mathbb{R}^m$ is the control input and
 120 $\mathbf{y} \in \mathbb{R}^p$ is the measured output. Since our model reduction procedure draws inspiration from

121 the form of Petrov-Galerkin reduced-order models, we begin by providing a brief review of
 122 the latter. We then introduce our framework in section 2.2.

123 **2.1. Petrov-Galerkin models.** As discussed in the introduction, Petrov-Galerkin reduced-
 124 order models are a class of models obtained by constraining the full-order dynamics in (2.1)
 125 to a linear subspace of \mathbb{R}^n . While Petrov-Galerkin models can also be obtained via nonlinear
 126 projection onto curved manifolds [24], here we constrain our attention to the more common
 127 case of linear projections. Given rank- r matrices $\Phi \in \mathbb{R}^{n \times r}$ and $\Psi \in \mathbb{R}^{n \times r}$ that define an
 128 *oblique* projection $\mathbb{P} = \Phi (\Psi^\top \Phi)^{-1} \Psi^\top$, the corresponding Petrov-Galerkin model for (2.1) is
 129 given by

$$130 \quad (2.2) \quad \begin{aligned} \frac{d\hat{\mathbf{x}}}{dt} &= \mathbb{P} \mathbf{f}(\mathbb{P}\hat{\mathbf{x}}, \mathbf{u}), \quad \hat{\mathbf{x}}(0) = \mathbb{P}\mathbf{x}_0 \\ \hat{\mathbf{y}} &= \mathbf{h}(\mathbb{P}\hat{\mathbf{x}}), \end{aligned}$$

131 where $\hat{\mathbf{x}}$ lies in the range of \mathbb{P} for all times. In the special case of $\Psi = \Phi$, the projection \mathbb{P} is
 132 orthogonal and the model (2.2) is referred to as a Galerkin model. While the state $\hat{\mathbf{x}} \in \mathbb{R}^n$
 133 is an n -dimensional vector (i.e., the same size of the original state \mathbf{x}), the dynamics (2.2) can
 134 be realized by an equivalent r -dimensional system

$$135 \quad (2.3) \quad \begin{aligned} \frac{d\hat{\mathbf{z}}}{dt} &= \Psi^\top \mathbf{f}(\Phi (\Psi^\top \Phi)^{-1} \hat{\mathbf{z}}, \mathbf{u}), \quad \hat{\mathbf{z}}(0) = \Psi^\top \mathbf{x}_0 \\ \hat{\mathbf{y}} &= \mathbf{h}(\Phi (\Psi^\top \Phi)^{-1} \hat{\mathbf{z}}) \end{aligned}$$

136 where the state vector $\hat{\mathbf{z}} = \Psi^\top \hat{\mathbf{x}}$ has dimension r . The primary challenge associated with com-
 137 puting accurate projection-based reduced-order models lies in identifying matrices Φ and Ψ
 138 that define appropriate projections \mathbb{P} . While there exist several methods to address this chal-
 139 lenge, these are often intrusive in the sense that they require access to the linearization of (2.1)
 140 and its adjoint [30, 25, 26]. In the next section, we present a non-intrusive model reduction
 141 formulation by allowing for the reduced-order dynamics to be independent of the full-order
 142 right-hand side \mathbf{f} .

143 **2.2. Non-intrusive optimization of projection operators and reduced-order dynamics.**

144 Here, we consider reduced-order models of the form

$$145 \quad (2.4) \quad G(\Phi, \Psi, \hat{\mathbf{f}}_r) = \begin{cases} \frac{d\hat{\mathbf{z}}}{dt} = \hat{\mathbf{f}}_r(\hat{\mathbf{z}}, \mathbf{u}), \quad \hat{\mathbf{z}}(0) = \Psi^\top \mathbf{x}_0 \\ \hat{\mathbf{y}} = \mathbf{h}(\Phi (\Psi^\top \Phi)^{-1} \hat{\mathbf{z}}) \end{cases}$$

146 It is instructive to observe that if $\hat{\mathbf{f}}_r(\hat{\mathbf{z}}, \mathbf{u}) = \Psi^\top \mathbf{f}(\Phi (\Psi^\top \Phi)^{-1} \hat{\mathbf{z}}, \mathbf{u})$ then (2.4) is the exact
 147 analog of the Petrov-Galerkin reduced-order model in (2.3). Instead, we let $\hat{\mathbf{f}}_r$ be a general
 148 function of the reduced-order state $\hat{\mathbf{z}}$ and of the input \mathbf{u} . So, while Petrov-Galerkin models
 149 are fully defined by (the span of) the matrices Φ and Ψ that define a projection onto a
 150 low-dimensional subspace, here we have additional degrees of freedom in the choice of the
 151 reduced-order dynamics. We shall see momentarily that this additional freedom allows us to
 152 proceed non-intrusively.

153 Within our framework, we seek reduced-order models of the form of (2.4) by minimizing
 154 the error between ground-truth observations \mathbf{y} coming from (2.1) and the predicted observa-
 155 tions $\hat{\mathbf{y}}$ given by (2.4). In order to convert this task into an appropriate optimization problem,
 156 it is useful to first identify the symmetries and constraints that are present in (2.4). We
 157 begin by observing that the system G in (2.4) is invariant with respect to a rotation and
 158 scaling of the basis matrix Φ . In fact, $G(\Phi\mathbf{R}, \Psi, \mathbf{f}_r) = G(\Phi, \Psi, \mathbf{f}_r)$ for any invertible matrix \mathbf{R}
 159 of size $r \times r$. It follows that the reduced-order system defined by (2.4) is a function of the
 160 r -dimensional subspace $V = \text{Range}(\Phi)$, rather than of the matrix representative Φ itself. In
 161 the mathematical statement of the problem we will make use of this symmetry and leverage
 162 the fact that r -dimensional subspaces of \mathbb{R}^n are elements of the Grassmann manifold $\mathcal{G}_{n,r}$. An
 163 analogous type of symmetry does *not* hold for Ψ . In fact, it can be easily verified that there
 164 exist invertible matrices \mathbf{S} such that $G(\Phi, \Psi\mathbf{S}, \mathbf{f}_r) \neq G(\Phi, \Psi, \mathbf{f}_r)$. While (2.4) does not enjoy
 165 any Ψ -symmetries, we still require Ψ to have full column rank (otherwise the product $\Psi^T\Phi$
 166 would be rank deficient). It is therefore natural to constrain Ψ to the Stiefel manifold $S_{n,r}$ of
 167 orthonormal (and, hence, full-rank) $n \times r$ matrices. Finally, in order to write an optimization
 168 problem where the gradient of the cost function with respect to all the parameters can be
 169 obtained in closed form, it is convenient to constrain the reduced-order dynamics \mathbf{f}_r to a form
 170 that lends itself to straightforward differentiation. Throughout this paper, we will let \mathbf{f}_r be a
 171 polynomial function of the reduced-order state $\hat{\mathbf{z}}$ and of the input \mathbf{u} as follows

$$172 \quad (2.5) \quad \mathbf{f}_r = \underbrace{\mathbf{A}_r \hat{\mathbf{z}} + \mathbf{B}_r \mathbf{u} + \mathbf{H}_r : \hat{\mathbf{z}}\hat{\mathbf{z}}^T + \mathbf{L}_r : \hat{\mathbf{z}}\mathbf{u}^T + \dots}_{:=\bar{\mathbf{f}}_r}$$

173 Here, capital letters denote reduced-order tensors that lie naturally on linear manifolds of
 174 appropriate dimension (e.g., $\mathbf{A}_r \in \mathbb{R}^{r \times r}$, $\mathbf{B}_r \in \mathbb{R}^{r \times m}$ and $\mathbf{H}_r \in \mathbb{R}^{r \times r \times r}$). In the interest of a
 175 more concise description of the mathematical formulation, we take $\mathbf{f}_r = \bar{\mathbf{f}}_r$ (see definition of $\bar{\mathbf{f}}_r$
 176 in the underbrace of equation (2.5)). Higher-order polynomial dynamics can be considered
 177 with minimal modification.

178 We are now ready to state the optimization problem that will give us an optimal reduced-
 179 order model of the form of (2.4). Given outputs $\mathbf{y}(t_i)$ sampled at times t_i along a trajectory
 180 generated from the full-order system (2.1), we seek a solution to

$$181 \quad (2.6) \quad \begin{aligned} \min_{(V, \Psi, \mathbf{A}_r, \mathbf{H}_r, \mathbf{B}_r) \in \mathcal{M}} \quad & J = \sum_{i=0}^{N-1} \|\mathbf{y}(t_i) - \hat{\mathbf{y}}(t_i)\|^2 \\ \text{subject to:} \quad & \frac{d\hat{\mathbf{z}}}{dt} = \bar{\mathbf{f}}_r(\hat{\mathbf{z}}, \mathbf{u}), \quad \hat{\mathbf{z}}(t_0) = \Psi^T \mathbf{x}(t_0) \\ & \hat{\mathbf{y}} = \mathbf{h}(\Phi(\Psi^T\Phi)^{-1}\hat{\mathbf{z}}) \\ & V = \text{Range}(\Phi) \end{aligned}$$

182 where $\mathcal{M} = \mathcal{G}_{n,r} \times S_{n,r} \times \mathbb{R}^{r \times r} \times \mathbb{R}^{r \times r \times r} \times \mathbb{R}^{r \times m}$ is the product manifold that defines our
 183 optimization domain.

184 **2.3. Gradient-based optimization on \mathcal{M} .** In order to solve the optimization problem (2.6)
 185 using a gradient-based algorithm, it is convenient to view \mathcal{M} as a submanifold of an *ambient-*

186 *space* manifold $\overline{\mathcal{M}}$ endowed with a Riemannian metric. We first define $\overline{\mathcal{M}}$ for our specific
187 case, then we discuss the Riemannian metric.

188 Since \mathcal{M} is a product manifold whose topology is the product topology of its individual
189 components, the ambient-space manifold $\overline{\mathcal{M}}$ can also be defined component-wise. Follow-
190 ing [1], we view the Stiefel manifold as an embedded submanifold of the vector space $\mathbb{R}^{n \times r}$,
191 and the Grassmann manifold $\mathcal{G}_{n,r}$ as a quotient manifold of the non-orthogonal Stiefel mani-
192 fold $\mathbb{R}_*^{n \times r}$ (which is the manifold of rank- r , but non necessarily orthonormal, matrices of size
193 $n \times r$). The manifolds $\mathbb{R}^{r \times r}$, $\mathbb{R}^{r \times r \times r}$ and $\mathbb{R}^{r \times m}$ are vector spaces that do not require any
194 special treatment, so $\overline{\mathcal{M}}$ may finally be defined as

$$195 \quad (2.7) \quad \overline{\mathcal{M}} = \mathbb{R}_*^{n \times r} \times \mathbb{R}^{n \times r} \times \mathbb{R}^{r \times r} \times \mathbb{R}^{r \times r \times r} \times \mathbb{R}^{r \times m}.$$

196

197 In order to define the gradient of the cost function with respect to the parameters, we now
198 endow the ambient-space manifold with a Riemannian metric, which will then be inherited
199 by the optimization manifold \mathcal{M} . Formally, a Riemannian metric $g^{\mathcal{M}}$ is a smooth family of
200 inner products $g_p^{\mathcal{M}}$ defined on the tangent spaces of the manifold \mathcal{M} ,

$$201 \quad (2.8) \quad g_p^{\mathcal{M}} : \mathcal{T}_p \mathcal{M} \times \mathcal{T}_p \mathcal{M} \rightarrow \mathbb{R},$$

202 where $\mathcal{T}_p \mathcal{M}$ denotes the tangent space of \mathcal{M} at a point $p \in \mathcal{M}$ [1]. The gradient ξ of the cost
203 function at $p \in \mathcal{M}$ is then defined as the element of the tangent space $\mathcal{T}_p \mathcal{M}$ that satisfies

$$204 \quad (2.9) \quad DJ[\eta] = g_p^{\mathcal{M}}(\xi, \eta), \quad \forall \eta \in \mathcal{T}_p \mathcal{M},$$

205 where $DJ[\eta]$ is the directional derivative. A metric for a product manifold can be defined as
206 the sum of the component metrics, so we can proceed component-wise as before. The metric
207 for the Stiefel manifold $S_{n,r}$ can be defined as

$$208 \quad (2.10) \quad g_{\Psi}^{S_{n,r}}(\xi, \eta) = \text{Tr}(\xi^T \eta), \quad \xi, \eta \in \mathcal{T}_{\Psi} S_{n,r},$$

209 which is the Euclidean metric inherited from the ambient space $\mathbb{R}^{n \times r}$ [1] and Tr denotes
210 the trace. A metric for the Grassmann manifold can be defined analogously, albeit paying
211 attention to the fact that the Grassmannian is an abstract manifold with non-unique matrix
212 representatives. In particular, given the ambient space metric

$$213 \quad (2.11) \quad g_{\Phi}^{\mathbb{R}_*^{n \times r}}(\xi, \eta) = \text{Tr}\left((\Phi^T \Phi)^{-1} \xi^T \eta\right), \quad \xi, \eta \in \mathcal{T}_{\Phi} \mathbb{R}_*^{n \times r}$$

214 we let the metric on $\mathcal{G}_{n,r}$ be defined as

$$215 \quad (2.12) \quad g_V^{\mathcal{G}_{n,r}}(\xi, \eta) = g_{\Phi}^{\mathbb{R}_*^{n \times r}}(\bar{\xi}_{\Phi}, \bar{\eta}_{\Phi}), \quad \xi, \eta \in \mathcal{T}_V, \quad \text{Range}(\Phi) = V.$$

216 It is worth observing that (2.12) is not yet suited for computation, since there exists an infinite
217 number of elements $\bar{\xi}_{\Phi}$ and $\bar{\eta}_{\Phi}$ of $\mathcal{T}_{\Phi} \mathbb{R}_*^{n \times r}$ that satisfy the equality. The ambiguity is resolved
218 by requiring $\bar{\xi}_{\Phi}$ and $\bar{\eta}_{\Phi}$ to lie on the *horizontal space*, which is a subspace of $\mathcal{T}_{\Phi} \mathbb{R}_*^{n \times r}$ where
219 one may identify unique $\bar{\xi}_{\Phi}$ and $\bar{\eta}_{\Phi}$ that satisfy (2.12). This unique vector $\bar{\xi}_{\Phi}$ is known as

220 the *horizontal lift* of ξ at Φ . A rigorous characterization of the horizontal space is provided
 221 in chapter 3 of [1], and the specific case of the Grassmann manifold is considered in example
 222 3.6.4 in the same reference. Finally, for the linear manifolds in the Cartesian product of \mathcal{M} ,
 223 we adopt the Euclidean metric (i.e., the usual tensor dot product).

224 Now that we have defined the ambient-space manifold $\overline{\mathcal{M}}$ and metrics on \mathcal{M} , we can
 225 approach the computation of the gradient of the cost function in terms of ambient-space
 226 matrix-valued objects, rather than abstract elements of the optimization manifold \mathcal{M} . In
 227 order to do so, we invoke the “canonical projection” [1]

$$228 \quad (2.13) \quad \pi : \widetilde{\mathcal{M}} \rightarrow \mathcal{M} : (\Phi, \Psi, \mathbf{A}_r, \mathbf{H}_r, \mathbf{B}_r) \mapsto (\text{Range}(\Phi), \Psi, \mathbf{A}_r, \mathbf{H}_r, \mathbf{B}_r),$$

229 where $\widetilde{\mathcal{M}} = \mathbb{R}_*^{n \times r} \times St_{n,r} \times \mathbb{R}^{r \times r} \times \mathbb{R}^{r \times r \times r} \times \mathbb{R}^{r \times m}$. Then, given our cost function $J : \mathcal{M} \rightarrow \mathbb{R}$,
 230 for any point $(V, \Psi, \mathbf{A}_r, \mathbf{H}_r, \mathbf{B}_r) \in \mathcal{M}$ we have

$$231 \quad (2.14) \quad J(V, \Psi, \mathbf{A}_r, \mathbf{H}_r, \mathbf{B}_r) = J(\pi(\Phi, \Psi, \mathbf{A}_r, \mathbf{H}_r, \mathbf{B}_r)) = \overline{J}(\Phi, \Psi, \mathbf{A}_r, \mathbf{H}_r, \mathbf{B}_r),$$

232 where $(\Phi, \Psi, \mathbf{A}_r, \mathbf{H}_r, \mathbf{B}_r) \in \widetilde{\mathcal{M}}$ and $V = \text{Range}(\Phi)$. If we view $\overline{J} : \overline{\mathcal{M}} \rightarrow \mathbb{R}$ as a function that
 233 sends elements of the ambient space to the reals, then equation (2.14) implies that J on \mathcal{M} is
 234 equal to the *restriction* of \overline{J} to $\widetilde{\mathcal{M}}$. This restriction ensures that the second argument of \overline{J} is
 235 an element of the Stiefel manifold (as opposed to a generic element of $\mathbb{R}^{n \times r}$). We henceforth
 236 refer to \overline{J} as the ambient-space cost function. It follows from standard results (see equations
 237 (3.37) and (3.39) in [1]) that

$$238 \quad (2.15) \quad (\overline{\nabla}_V \overline{J}_\Phi, \nabla_\Psi J, \nabla_{\mathbf{A}_r} J, \nabla_{\mathbf{H}_r} J, \nabla_{\mathbf{B}_r} J) = (\nabla_\Phi \overline{J}, \mathbb{P}_\Psi \nabla_\Psi \overline{J}, \nabla_{\mathbf{A}_r} \overline{J}, \nabla_{\mathbf{H}_r} \overline{J}, \nabla_{\mathbf{B}_r} \overline{J}),$$

239 where the gradient of \overline{J} is evaluated at $(\Phi, \Psi, \mathbf{A}_r, \mathbf{H}_r, \mathbf{B}_r) \in \widetilde{\mathcal{M}}$, and the gradient of J is
 240 evaluated at $(V, \Psi, \mathbf{A}_r, \mathbf{H}_r, \mathbf{B}_r) \in \mathcal{M}$ with $V = \text{Range}(\Phi)$. Here, $\overline{\nabla}_V \overline{J}_\Phi$ denotes the horizontal
 241 lift of $\nabla_V J$ at Φ , \mathbb{P}_Ψ denotes the projection onto the tangent space of $St_{n,r}$ at Ψ (see example
 242 3.6.2 in [1]) and we remark that $\nabla_\Psi \overline{J}$ is an element of the tangent space of $\mathbb{R}^{n \times r}$ at Ψ . In
 243 summary, the equation above states that the gradient of the cost function with respect to the
 244 abstract optimization parameters can be computed in terms of the gradient of the ambient-
 245 space cost function. Conveniently, our model reduction formulation allows for the ambient-
 246 space gradient to be computed in closed form, and this result is stated in the proposition below.
 247 Importantly, we shall see that the computation of the gradient does not require querying
 248 the full-order model (2.1). That is, the gradient can be computed non-intrusively. Once the
 249 ambient-space gradient is available, the gradient with respect to the optimization parameters is
 250 computed using (2.15) by libraries such as Pymanopt [36] in Python or Manopt [7] in MATLAB.

251 **Proposition 2.1 (Ambient-space gradient).** *Let problem (2.6) be written as an equivalent*
 252 *unconstrained optimization problem with ambient-space Lagrangian $\overline{L} : \overline{\mathcal{M}} \rightarrow \mathbb{R}$ defined as*

$$253 \quad (2.16) \quad \overline{L}(\Phi, \overline{\Psi}, \mathbf{A}_r, \mathbf{H}_r, \mathbf{B}_r) = \sum_{i=0}^{N-1} \left\{ \overline{J}_i + \int_{t_0}^{t_i} \lambda_i^\top \left(\frac{d\hat{\mathbf{z}}}{dt} - \mathbf{A}_r \hat{\mathbf{z}} - \mathbf{H}_r : \hat{\mathbf{z}} \hat{\mathbf{z}}^\top - \mathbf{B}_r \mathbf{u} \right) dt \right. \\ \left. + \lambda_i(t_0)^\top \left(\hat{\mathbf{z}}(t_0) - \overline{\Psi}^\top \mathbf{x}(t_0) \right) \right\},$$

254 where $\bar{J}_i = \|\mathbf{y}(t_i) - \mathbf{h}\left(\Phi\left(\bar{\Psi}^\top\Phi\right)^{-1}\hat{\mathbf{z}}(t_i)\right)\|^2$ and $\lambda_i(t) \in \mathbb{R}^r$ with $t \in [t_0, t_i]$ is the i th Lagrange
 255 multiplier. Defining $\mathbf{e}(t_i) := \mathbf{y}(t_i) - \mathbf{h}\left(\Phi\left(\bar{\Psi}^\top\Phi\right)^{-1}\hat{\mathbf{z}}(t_i)\right)$ and $\mathbf{C}_{j,k} := \partial\mathbf{h}_j/\partial\mathbf{x}_k$, the gradients
 256 of the ambient-space Lagrangian with respect to its parameters are given below,

$$257 \quad (2.17) \quad \nabla_{\Phi}\bar{L} = \left\{ -2 \sum_{i=0}^{N-1} \left(\mathbf{I} - \bar{\Psi}(\Phi^\top\bar{\Psi})^{-1}\Phi^\top \right) \mathbf{C}(t_i)^\top \mathbf{e}(t_i) \hat{\mathbf{z}}(t_i)^\top \left(\bar{\Psi}^\top\Phi \right)^{-1} \right\} (\Phi^\top\Phi)$$

$$258 \quad (2.18) \quad \nabla_{\bar{\Psi}}\bar{L} = \sum_{i=0}^{N-1} \left(2\Phi\left(\bar{\Psi}^\top\Phi\right)^{-1}\hat{\mathbf{z}}(t_i)\mathbf{e}(t_i)^\top\mathbf{C}(t_i)\Phi\left(\bar{\Psi}^\top\Phi\right)^{-1} - \mathbf{x}(t_0)\lambda_i(t_0)^\top \right)$$

$$259 \quad (2.19) \quad \nabla_{\mathbf{A}_r}\bar{L} = - \sum_{i=0}^{N-1} \int_{t_0}^{t_i} \lambda_i \hat{\mathbf{z}}^\top dt$$

$$260 \quad (2.20) \quad \nabla_{\mathbf{H}_r}\bar{L} = - \sum_{i=0}^{N-1} \int_{t_0}^{t_i} \lambda_i \otimes \hat{\mathbf{z}} \otimes \hat{\mathbf{z}} dt$$

$$261 \quad (2.21) \quad \nabla_{\mathbf{B}_r}\bar{L} = - \sum_{i=0}^{N-1} \int_{t_0}^{t_i} \lambda_i \mathbf{u}^\top dt,$$

262 where the Lagrange multiplier $\lambda_i(t)$ satisfies the reduced-order adjoint equation

$$263 \quad (2.22) \quad -\frac{d\lambda_i}{dt} = [\partial_{\hat{\mathbf{z}}}\bar{\mathbf{f}}_r(\hat{\mathbf{z}})]^\top \lambda_i, \quad \lambda_i(t_i) = 2(\Phi^\top\bar{\Psi})^{-1}\Phi^\top\mathbf{C}(t_i)^\top\mathbf{e}(t_i), \quad t \in [t_0, t_i].$$

264 *Proof.* The proof relies on calculus of variations. At a local minimum $p \in \bar{\mathcal{M}}$, the following
 265 must hold for every vector $\xi \in \mathcal{T}_p\bar{\mathcal{M}}$,

$$266 \quad (2.23) \quad g_p^{\bar{\mathcal{M}}}(\nabla_p\bar{L}, \xi) = D_p\bar{L}[\xi] = \partial_p\bar{L}[\xi] + \partial_{\hat{\mathbf{z}}}\bar{L} \cdot D_p\hat{\mathbf{z}}[\xi] + \sum_{i=0}^{N-1} (\partial_{\lambda_i}\bar{L} \cdot D_p\lambda_i[\xi]) = 0,$$

267 where $g_p^{\bar{\mathcal{M}}}$ denotes the ambient-space metric on $\bar{\mathcal{M}}$ at p (which we have defined component-
 268 wise earlier in section 2.3). By enforcing $\partial_{\hat{\mathbf{z}}}\bar{L}[\boldsymbol{\eta}] = 0$ for all $\boldsymbol{\eta}$, the equality above reduces to
 269

$$270 \quad (2.24) \quad g_p^{\bar{\mathcal{M}}}(\nabla_p\bar{L}, \xi) = \partial_p\bar{L}[\xi] = 0,$$

271 since $\partial_{\lambda_i}\bar{L} = 0$ for all i by virtue of the fact that λ_i is a Lagrange multiplier. We begin by
 272 showing that the reduced-order adjoint equation (2.22) enforces $\partial_{\hat{\mathbf{z}}}\bar{L}[\boldsymbol{\eta}] = 0$ for all $\boldsymbol{\eta}$. Given
 273 the ambient-space Lagrangian \bar{L} , we have

$$(2.25) \quad \partial_{\hat{\mathbf{z}}}\bar{L}[\boldsymbol{\eta}] = \sum_{i=0}^{N-1} \left\{ -2\mathbf{e}(t_i)^\top\mathbf{C}(t_i)\Phi\left(\bar{\Psi}^\top\Phi\right)^{-1}\boldsymbol{\eta}(t_i) + \lambda_i^\top\boldsymbol{\eta} \Big|_{t_0}^{t_i} - \int_{t_0}^{t_i} \left(\frac{d\lambda_i^\top}{dt} + \lambda_i^\top[\partial_{\hat{\mathbf{z}}}\bar{\mathbf{f}}_r(\hat{\mathbf{z}})] \right) \boldsymbol{\eta} dt \right. \\ \left. + \lambda_i(t_0)^\top\boldsymbol{\eta}(t_0) \right\} = 0,$$

275 where we have used integration by parts on the time-derivative term. For each $i > 0$, the
 276 terms $\lambda_i(t_0)^\top \eta(t_0)$ cancel out and the summand vanishes thanks to equation (2.22). Similarly,
 277 when $i = 0$, the second and third terms in the sum vanish and the summand is equal to zero
 278 for $\lambda_0(t_0) = 2(\Phi^\top \Psi)^{-1} \Phi^\top C(t_0)^\top e(t_0)$. We now derive the gradient of \bar{L} with respect to Φ .
 279 The partial derivative of \bar{L} with respect to Φ in the direction of ξ is given by

$$280 \quad (2.26) \quad \partial_{\Phi} \bar{L}[\xi] = -2 \sum_{i=0}^{N-1} e(t_i)^\top C(t_i) \left(\xi \left(\bar{\Psi}^\top \Phi \right)^{-1} - \Phi \left(\bar{\Psi}^\top \Phi \right)^{-1} \bar{\Psi}^\top \xi \left(\bar{\Psi}^\top \Phi \right)^{-1} \right) \hat{z}(t_i),$$

281 where we have used the identity $D_{\Phi} \left(\bar{\Psi}^\top \Phi \right)^{-1} [\xi] = - \left(\bar{\Psi}^\top \Phi \right)^{-1} \bar{\Psi}^\top \xi \left(\bar{\Psi}^\top \Phi \right)^{-1}$. Using (2.24),
 282 and recalling the definition of the ambient-space metric on $\mathbb{R}_*^{n \times r}$ (2.11), we recover the gradient
 283 in (2.17). The other gradients can be obtained similarly and the proof is concluded. ■

284 Another ingredient that is necessary for gradient-based manifold optimization is the con-
 285 cept of a *retraction*. This is a map $R_p : \mathcal{T}_p \mathcal{M} \rightarrow \mathcal{M}$ that satisfies $R_p(0) = p$ and $DR_p(0) =$
 286 $I_{\mathcal{T}_p \mathcal{M}}$, where $I_{\mathcal{T}_p \mathcal{M}}$ is the identity map on the tangent space $\mathcal{T}_p \mathcal{M}$ [1]. The use of this map
 287 allows us to generalize the concept of moving in the direction of the gradient on a nonlinear
 288 manifold: for instance, given a point $p \in \mathcal{M}$ and the gradient $\xi \in \mathcal{T}_p \mathcal{M}$ of a function f defined
 289 on \mathcal{M} , the next iterate in the direction of the gradient is given by $R_p(p - \alpha \xi) \in \mathcal{M}$, where α
 290 is some learning rate. In other words, the retraction allows us to guarantee that all iterates
 291 generated by a gradient flow lie on the manifold. Valid retractions for both the Stiefel and
 292 Grassmann manifolds are given by the QR decomposition (see examples 4.1.3 and 4.1.5 in
 293 [1]), while for linear manifolds the retraction is simply the identity map. Lastly, we point out
 294 that second-order gradient-based algorithms (e.g., conjugate gradient) require the concept of
 295 *vector transport*. This is described thoroughly in section 8.1 of [1]. Gradient-based algorithms
 296 on nonlinear manifolds are well-understood and readily available in libraries such as `Pymanopt`
 297 [36] and `Manopt` [7]. Metrics, retractions and vector transports are conveniently handled by
 298 these packages, and a user simply needs to provide routines to evaluate the cost function and
 299 the ambient-space gradient provided in Proposition 2.1.

300 **2.4. Computational considerations.** In this subsection, we discuss the efficient computa-
 301 tion of the ambient-space gradient presented in Proposition 2.1. We then provide an algorithm
 302 and estimate of the computational cost.

303 In order to efficiently calculate the gradient, it is useful to manipulate the expressions
 304 in (2.19)-(2.21) into a form that is more suitable for computation. In particular, since the
 305 integrands in (2.19)-(2.21) are linear in λ_i , we can write, e.g.,

$$306 \quad (2.27) \quad \sum_{i=0}^{N-1} \int_{t_0}^{t_i} \lambda_i(t) \hat{z}(t)^\top dt = \sum_{i=1}^{N-1} \int_{t_{i-1}}^{t_i} \xi_i(t) \hat{z}(t)^\top dt, \quad \xi_i(t) = \sum_{j=i}^{N-1} \lambda_j(t),$$

307 where $\xi_i(t)$ may be understood as a cumulative adjoint variable that can be computed by
 308 time-stepping the adjoint equation (2.22) backward in time from t_{N-1} to t_0 . Then, according
 309 to the equation above, the gradients in (2.19)-(2.21) can be conveniently computed as a sum of
 310 integrals over short temporal intervals $[t_{i-1}, t_i]$, as opposed to a sum of integrals over temporal

311 intervals of increasing length $[t_0, t_i]$. Having defined $\xi_i(t)$, the term $\sum_{i=0}^{N-1} \mathbf{x}(t_0) \lambda_i(t_0)^\top =$
 312 $\mathbf{x}(t_0) \xi_0(t_0)^\top$ in equation (2.18) can also be evaluated efficiently. These details are illustrated
 313 in Algorithm 2.1.

Algorithm 2.1 Compute ambient-space gradient in Proposition 2.1

Input: Training data $\{\mathbf{y}(t_i)\}_{i=0}^{N-1}$, initial condition $\mathbf{x}(0)$ of the full-order model, input $\mathbf{u}(t)$
 and a point $(V, \Psi, \mathbf{A}_r, \mathbf{H}_r, \mathbf{B}_r) \in \mathcal{M}$, with some matrix representative Φ such that
 $\text{Range}(\Phi) = V$.

Output: Ambient-space gradients (2.17)-(2.21) in Proposition 2.1

- 1: Initialize arrays to store $\nabla_{\Phi} \bar{L}$, $\nabla_{\Psi} \bar{L}$, $\nabla_{\mathbf{A}_r} \bar{L}$, $\nabla_{\mathbf{H}_r} \bar{L}$ and $\nabla_{\mathbf{B}_r} \bar{L}$
 - 2: Compute the ROM solution $\hat{\mathbf{z}}(t)$ with initial condition $\Psi^\top \mathbf{x}(0)$ and external input $\mathbf{u}(t)$
 - 3: Store values $\hat{\mathbf{z}}(t_i)$ (with $i \in \{0, 1, \dots, N-1\}$), then compute $\mathbf{e}(t_i)$ and $\mathbf{C}(t_i)$ defined in Proposition 2.1
 - 4: **for** $i \in \{N-1, N-2, \dots, 1\}$ **do**
 - 5: Update $\nabla_{\Phi} \bar{L} \leftarrow \nabla_{\Phi} \bar{L} - 2 \left(\mathbf{I} - \Psi (\Phi^\top \Psi)^{-1} \Phi^\top \right) \mathbf{C}(t_i)^\top \mathbf{e}(t_i) \hat{\mathbf{z}}(t_i)^\top (\Psi^\top \Phi)^{-1} (\Phi^\top \Phi)$
 - 6: Update $\nabla_{\Psi} \bar{L} \leftarrow \nabla_{\Psi} \bar{L} + 2 \Phi (\Psi^\top \Phi)^{-1} \hat{\mathbf{z}}(t_i) \mathbf{e}(t_i)^\top \mathbf{C}(t_i) \Phi (\Psi^\top \Phi)^{-1}$
 - 7: Compute $\xi_i(t)$ (see (2.27)) for $t \in [t_{i-1}, t_i]$ by integrating the adjoint equation (2.22) backward in time with final condition $\xi_i(t_i) = \xi_{i+1}(t_i) + 2 (\Phi^\top \Psi)^{-1} \Phi^\top \mathbf{C}(t_i)^\top \mathbf{e}(t_i)$
 - 8: Update $\nabla_{\mathbf{A}_r} \bar{L} \leftarrow \nabla_{\mathbf{A}_r} \bar{L} - \int_{t_{i-1}}^{t_i} \xi_i(t) \hat{\mathbf{z}}(t)^\top dt$ using, e.g., Gaussian quadrature
 - 9: Update $\nabla_{\mathbf{H}_r} \bar{L} \leftarrow \nabla_{\mathbf{H}_r} \bar{L} - \int_{t_{i-1}}^{t_i} \xi_i(t) \otimes \hat{\mathbf{z}}(t) \otimes \hat{\mathbf{z}}(t) dt$
 - 10: Update $\nabla_{\mathbf{B}_r} \bar{L} \leftarrow \nabla_{\mathbf{B}_r} \bar{L} - \int_{t_{i-1}}^{t_i} \xi_i(t) \mathbf{u}(t)^\top dt$
 - 11: **end for**
 - 12: Set $\xi_0(t_0) \leftarrow \xi_1(t_0) + 2 (\Phi^\top \Psi)^{-1} \Phi^\top \mathbf{C}(t_0)^\top \mathbf{e}(t_0)$
 - 13: Update $\nabla_{\Phi} \bar{L} \leftarrow \nabla_{\Phi} \bar{L} - 2 \left(\mathbf{I} - \Psi (\Phi^\top \Psi)^{-1} \Phi^\top \right) \mathbf{C}(t_0)^\top \mathbf{e}(t_0) \hat{\mathbf{z}}(t_0)^\top (\Psi^\top \Phi)^{-1}$
 - 14: Update $\nabla_{\Psi} \bar{L} \leftarrow \nabla_{\Psi} \bar{L} + 2 \Phi (\Psi^\top \Phi)^{-1} \hat{\mathbf{z}}(t_0) \mathbf{e}(t_0)^\top \mathbf{C}(t_0) \Phi (\Psi^\top \Phi)^{-1} - \mathbf{x}(t_0) \xi_0(t_0)^\top$
-

314 As far as computational cost is concerned, the algorithm scales with the number of snap-
 315 shots N along a training trajectory, the ROM dimension r , the polynomial order of the ROM
 316 dynamics p , the size of the full-order state n , the number of time steps n_t to integrate the
 317 ROM from time t_i to t_{i+1} , and the number of quadrature points n_q used to estimate the
 318 temporal integrals. Given the presence of a for loop with $N-1$ iterations (line 4 in the
 319 algorithm), the overall cost of is $O(Nc)$, where c is the cost associated with each for loop
 320 iteration i . The major contributors to the latter are the presence of matrix-vector products
 321 involving Φ and Ψ (which we recall being matrices of size $n \times r$), the need to integrate the
 322 reduced-order adjoint dynamics backward in time (line 7 in the algorithm), and the evaluation
 323 of the integrals involving r -dimensional tensor products (see, e.g., line 9). The cost of matrix-
 324 vector products involving Φ and Ψ is $O(nr)$, the cost associated with integrating the adjoint
 325 equations is $O(n_t r^{p+1})$, where n_t is the number of time steps taken from t_i to t_{i+1} , and the
 326 evaluation of the integrals scales as $O(n_q r^{p+1})$, where n_q is the number of quadrature points.
 327 Usually, $n_q \ll n_t$ (this is the case if we use high-order Gaussian quadrature), so an estimate
 328 of the cost per for-loop iteration is given by $O(nr + n_t r^{p+1})$. In very high-dimensional sys-

329 tems where n is larger than $O(n_t r^p)$, the cost per iteration is dominated by the matrix-vector
 330 products involving Φ and Ψ , otherwise it is dominated by the ROM time stepper.

331 **2.5. Connection with existing methods.** While our model reduction framework shares
 332 similarities with several existing methods, we would like to emphasize a natural connection
 333 with the recently-developed Trajectory-based Optimization for Oblique Projections (TrOOP)
 334 [25] and the Operator Inference framework introduced in [28].

335 TrOOP is a model reduction framework whereby a Petrov-Galerkin reduced-order model
 336 of the form (2.2) is obtained by optimizing the projection operator \mathbb{P} against trajectories of the
 337 full-order model (2.1). More specifically, given r -dimensional subspaces $V = \text{Range}(\Phi)$ and
 338 $W = \text{Range}(\Psi)$, TrOOP seeks an optimal \mathbb{P} by solving the following optimization problem

$$339 \quad (2.28) \quad \min_{(V,W) \in \mathcal{M}_{\text{TrOOP}}} J_{\text{TrOOP}} = \sum_{i=0}^{N-1} \|\mathbf{y}(t_i) - \hat{\mathbf{y}}(t_i)\|^2$$

340 subject to (2.2) (or, equivalently, to (2.3)), where $\mathcal{M}_{\text{TrOOP}} = \mathcal{G}_{n,r} \times \mathcal{G}_{n,r}$ is the product of
 341 two Grassmann manifolds. While the cost function (2.28) is the same as the one in (2.6),
 342 solving the optimization problem (2.28) is intrusive because TrOOP constrains the reduced-
 343 order dynamics to be the Petrov-Galerkin projection of the full-order dynamics. Consequently,
 344 computing the gradient of the cost function J_{TrOOP} with respect to the parameters requires
 345 differentiating through the dynamics \mathbf{f} in (2.1). This can be seen by deriving the gradient in a
 346 way analogous to that of Proposition 2.1, or alternatively, following Proposition 4.3 in [25]. As
 347 previously discussed, not all black box solvers allow for easy differentiation of the governing
 348 equations so, for this reason, solving the TrOOP optimization problem can be infeasible in
 349 some applications.

350 Operator Inference, on the other hand, is a non-intrusive model reduction framework
 351 that seeks a reduced-order model by orthogonally projecting the data onto a low-dimensional
 352 subspace and then fitting the reduced-order dynamics. This subspace is typically chosen as
 353 the span of the leading Proper Orthogonal Decomposition (POD) modes associated with some
 354 representative data set generated from (2.1). In particular, given a full-order trajectory $\mathbf{x}(t_i)$
 355 sampled from (2.1) at times t_i , the time-derivative $d\mathbf{x}(t_i)/dt$, the input $\mathbf{u}(t_i)$, a r -dimensional
 356 subspace spanned by $\Phi \in \mathbb{R}^{n \times r}$, and some parameterization of the reduced-order dynamics
 357 (e.g., $\mathbf{f}_r = \mathbf{A}_r \hat{\mathbf{z}} + \mathbf{H}_r : \hat{\mathbf{z}} \hat{\mathbf{z}}^\top + \mathbf{B}_r \mathbf{u}$), Operator Inference solves

$$358 \quad (2.29) \quad \min_{(\mathbf{A}_r, \mathbf{H}_r, \mathbf{B}_r) \in \mathcal{M}_{\text{OpInf}}} J_{\text{OpInf}} = \sum_{i=0}^{N-1} \left\| \frac{d\hat{\mathbf{z}}(t_i)}{dt} - \mathbf{A}_r \hat{\mathbf{z}}(t_i) - \mathbf{H}_r : \hat{\mathbf{z}}(t_i) \hat{\mathbf{z}}(t_i)^\top - \mathbf{B}_r \mathbf{u}(t_i) \right\|^2,$$

359 where $\hat{\mathbf{z}}(t_i) = \Phi^\top \mathbf{x}(t_i)$ and $\mathcal{M}_{\text{OpInf}} = \mathbb{R}^{r \times r} \times \mathbb{R}^{r \times r \times r} \times \mathbb{R}^{r \times m}$. As observed in [28], equa-
 360 tion (2.29) can be conveniently written as a linear least-squares problem whose solution is
 361 obtained via the Moore-Penrose inverse rather than via iterative gradient-based algorithms.
 362 Furthermore, given the least-squares nature of the problem, it is straightforward to add reg-
 363 ularization (e.g., to promote stability and/or avoid overfitting) by penalizing the Frobenius
 364 norm of the parameters [21, 34]. While Operator Inference offers a convenient non-intrusive
 365 model reduction platform, it may suffer from the fact that it maps the high-dimensional data

366 onto a low-dimensional space via orthogonal projection. We shall see that this can lead to
 367 inaccurate models if the full-order dynamics exhibit transient growth (e.g., due to non-normal
 368 mechanisms).

369 It is now clear that our model reduction framework merges concepts from both TrOOP
 370 and Operator Inference. Specifically: TrOOP seeks optimal projections while constraining
 371 the reduced-order dynamics to be of Petrov-Galerkin form, Operator Inference seeks optimal
 372 reduced-order dynamics while constraining the projection operator to be orthogonal and onto
 373 the span of POD modes, and our formulation simultaneously seeks optimal projections and
 374 optimal reduced-order dynamics. Moving forward, we call our formulation “Non-intrusive
 375 Trajectory-based optimization of Reduced-Order Models” (NiTROM). In closing this section,
 376 it is also worth mentioning that NiTROM solves an optimization problem similar in spirit
 377 to the one in “low-rank dynamic mode decomposition” [33], where the encoder and decoder
 378 are taken to be elements of the Grassmann manifold, and the reduced-order dynamics are
 379 assumed to be linear and discrete in time. Furthermore, by viewing the projection operator as
 380 a linear autoencoder, we can find several connections between NiTROM and existing intrusive
 381 and non-intrusive model reduction formulations that rely on (usually nonlinear) autoencoders
 382 parameterized by neural networks. Recent examples may be found in [13, 10, 24], although,
 383 to the best of our understanding, the only autoencoder architecture that defines a nonlinear
 384 projection onto a curved manifold is presented in [24].

385 **3. Application to a toy model.** In this section, we apply NiTROM to a three-dimensional
 386 toy model, and we compare with the intrusive TrOOP and POD Galerkin formulations and
 387 the non-intrusive Operator Inference. The model is governed by the following equations

$$388 \quad (3.1) \quad \dot{x}_1 = -x_1 + \nu x_1 x_3 + u$$

$$389 \quad (3.2) \quad \dot{x}_2 = -2x_2 + \nu x_2 x_3 + u$$

$$390 \quad (3.3) \quad \dot{x}_3 = -5x_3 + u$$

$$391 \quad (3.4) \quad y = x_1 + x_2 + x_3,$$

392 where $\dot{x}_1 = dx_1/dt$ and ν is a parameter. If ν is small, then these dynamics are effectively
 393 linear and governed by a normal (in fact, diagonal) linear operator. Conversely, if ν is large,
 394 the dynamics become particularly tedious [25, 26]: not only are they more heavily nonlinear,
 395 but the nonlinearity is such that the rapidly-decaying state x_3 has a large impact on the
 396 remaining states. Systems where low-energy (or rapidly-decaying) states have a large impact
 397 on the remaining states are precisely those where ROMs obtained via orthogonal projection
 398 are more likely to give inaccurate predictions. In order to demonstrate this phenomenon, we
 399 consider two separate cases, $\nu = 5$ and $\nu = 20$, and we seek two-dimensional ROMs capable of
 400 predicting the time history of the measured output y in response to step inputs $u(t) = \gamma H(t)$,
 401 where $H(t)$ is the Heaviside step function centered at $t = 0$, and $\gamma \in (0, 1/4)$. Given the
 402 quadratic nature of the full-order dynamics, we seek quadratic ROMs of the form

$$403 \quad (3.5) \quad \frac{d\hat{\mathbf{z}}}{dt} = \mathbf{A}_r \hat{\mathbf{z}} + \mathbf{H}_r : \hat{\mathbf{z}}\hat{\mathbf{z}}^\top + \mathbf{\Psi}^\top \mathbf{u}$$

$$404 \quad (3.6) \quad \hat{y} = \mathbf{C}\Phi (\mathbf{\Psi}^\top \Phi)^{-1} \hat{\mathbf{z}},$$

405 where $\mathbf{C} = [1\ 1\ 1]$ is a row vector and $\mathbf{u} = (u, u, u)$.

406 For both cases, $\nu = 5$ and $\nu = 20$, we train the models as follows. We collect $y(t)$ from
 407 $N_{\text{traj}} = 4$ step responses generated with $\gamma \in \{0.01, 0.1, 0.2, 0.248\}$ and initialized from rest.
 408 For each trajectory, we sample y at $N = 20$ equally-spaced times $t_i \in [0, 10]$. The cost function
 409 for NiTROM and TrOOP is

$$410 \quad (3.7) \quad J = \sum_{j=0}^{N_{\text{traj}}-1} \frac{1}{\alpha_j} \sum_{i=0}^{N-1} \|y^{(j)}(t_i) - \hat{y}^{(j)}(t_i)\|^2,$$

411 with $\alpha_j = N_{\text{traj}} N \|\mathbf{C}\bar{\mathbf{x}}^{(j)}\|^2$, where $\bar{\mathbf{x}}^{(j)}$ is the exact steady state that arises in response to the
 412 step input magnitude $\gamma^{(j)}$. (The steady state is computed analytically for simplicity, but it
 413 could just as easily have been computed via time-stepping since all steady states considered
 414 herein are linearly stable.) For both methods, the optimization was performed using the con-
 415 jugate gradient algorithm available in `Pymanopt` [36], with the ambient-space gradient defined
 416 following Proposition 2.1. Both methods were initialized with $\Psi = \Phi$ given by the leading
 417 two POD modes computed from the four training step responses. Additionally, NiTROM was
 418 provided with initial reduced-order tensors computed via Galerkin projection of the full-order
 419 dynamics onto the POD modes. The cost function for Operator Inference is

$$420 \quad (3.8) \quad J_{\text{OpInf}} = \sum_{j=0}^{N_{\text{traj}}-1} \frac{1}{\alpha_j} \sum_{i=0}^{N-1} \left\| \frac{d\hat{\mathbf{z}}^{(j)}(t_i)}{dt} - \mathbf{A}_r \hat{\mathbf{z}}^{(j)}(t_i) - \mathbf{H}_r : \hat{\mathbf{z}}^{(j)}(t_i) \hat{\mathbf{z}}^{(j)}(t_i)^\top - \Phi^\top \mathbf{u}^{(j)}(t_i) \right\|^2 \\ + \lambda \|\text{Mat}(\mathbf{H}_r)\|_F^2,$$

421 where Φ are the POD modes that we just described, $\hat{\mathbf{z}} = \Phi^\top \mathbf{x}$, $\text{Mat}(\mathbf{H}_r)$ denotes the matri-
 422 cization of the third-order tensor \mathbf{H}_r and λ is the regularization parameter. In both cases
 423 ($\nu = 5$ and $\nu = 20$) $\lambda \approx 10^{-7}$, and the chosen λ is (approximately) the one that yields the
 424 best possible Operator Inference model, as measured by the cost function J in (3.7). Also, it
 425 is worth mentioning that the time-derivative of the reduced-order state $d\hat{\mathbf{z}}(t_i)/dt$ is computed
 426 exactly. That is, $d\hat{\mathbf{z}}(t_i)/dt = \Phi^\top \mathbf{f}(\mathbf{x}(t_i))$, where \mathbf{f} denotes the right-hand side of the full-order
 427 dynamics and $\mathbf{x}(t_i)$ is the training full-order snapshot whose POD coefficients are $\hat{\mathbf{z}}(t_i)$.

428 The models were tested by generating 100 step-response trajectories with γ sampled uni-
 429 formly at random from the interval $(0, 1/4)$. The results are shown in figure 1a for both values
 430 of ν , where the average error over trajectories is defined as

$$431 \quad (3.9) \quad e(t) = \frac{1}{N_{\text{traj}}} \sum_{j=0}^{N_{\text{traj}}-1} \frac{1}{\alpha_j} \|y^{(j)}(t) - \hat{y}^{(j)}(t)\|^2,$$

432 with α_j as in (3.7). Figure 1a shows that all models are very accurate when $\nu = 5$. This
 433 is expected, since we have seen that for lower values of ν (and for the moderate step input
 434 magnitudes we are considering here), the dynamics of the full-order model are effectively linear
 435 and (more importantly) governed by a normal operator. Therefore, accurate ROMs can be
 436 obtained via orthogonal projection. The accuracy of all the models can also be appreciated
 437 in figure 2a, where we see the time history of the output y in response to a sinusoidal input

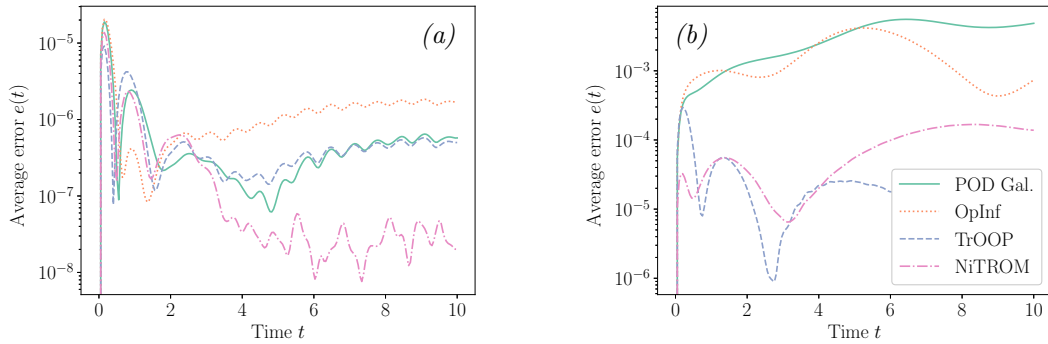


Figure 1: Toy model: (a) average testing error (3.9) for $\nu = 5$ (normal dynamics). (b) Analog for $\nu = 20$ (non-normal dynamics).

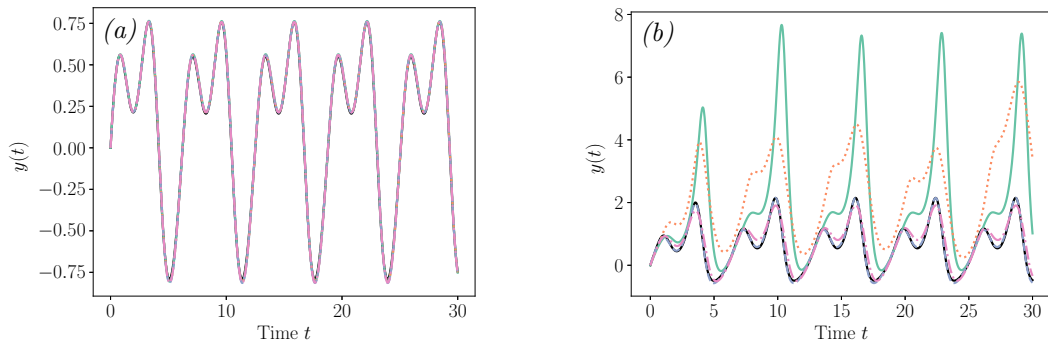


Figure 2: Toy model: time history of the output y in response to a sinusoidal input $u(t) = 0.45(\sin(t) + \cos(2t))$ with (a) $\nu = 5$ (normal dynamics) and (b) $\nu = 20$ (non-normal dynamics). The black continuous line is the ground-truth given by the full-order model. The rest of the legend is in figure 1.

438 (recall that we have not trained on sinusoids). By contrast, as we increase ν to 20, we start
 439 to observe some loss in predictive accuracy, particularly from the models (POD Galerkin and
 440 Operator Inference) that rely on orthogonal projections. This can be seen in figure 1b, and,
 441 even more convincingly, in figure 2b. In the latter, we see that while NiTROM and TrOOP
 442 provide a very good estimate of the output y in response to a sinusoidal input, the POD
 443 Galerkin and Operator Inference models struggle to do so. This must be attributed to the
 444 fact that TrOOP and NiTROM identify ROMs via oblique projection, while the other two
 445 methods use orthogonal projections.

446 For completeness, we also show the decay of the loss function versus conjugate gradient
 447 iterations for both TrOOP and NiTROM in figure 3. In particular, we observe that in both
 448 cases ($\nu = 5$ and $\nu = 20$), NiTROM attains a lower loss function value than TrOOP. However,
 449 in the $\nu = 20$ case, TrOOP reaches the stopping criterion $\|\nabla J\| \leq 10^{-6}$ much faster than
 450 NiTROM. Presumably, this is due to the fact that NiTROM's optimization landscape is "less

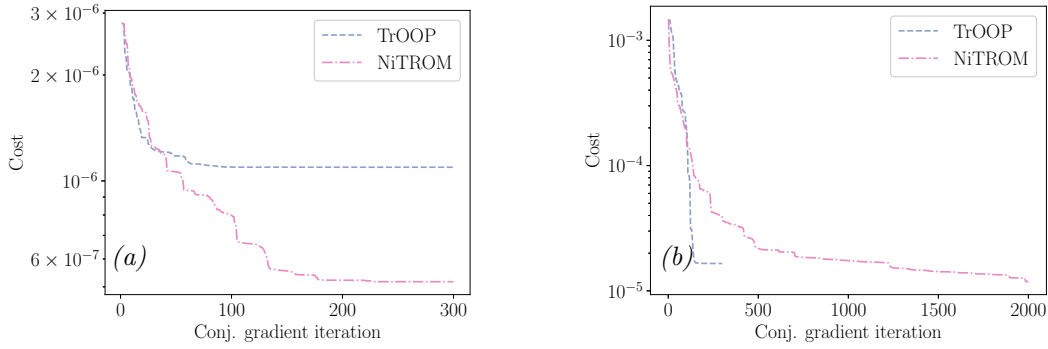


Figure 3: Toy model: cost function value (3.7) versus conjugate gradient iteration for (a) $\nu = 5$ and (b) $\nu = 20$.

451 friendly” than TrOOP’s, as NiTROM admits a larger class of solutions. In fact, while the
 452 larger number of parameters in NiTROM allows for a wider class of reduced-order models, it
 453 may also make it more difficult for the optimizer to find a “good” local minimum.

454 **4. Application to the complex Ginzburg-Landau (CGL) equation.** In this section we
 455 consider the complex Ginzburg-Landau (CGL) equation

$$456 \quad (4.1) \quad \frac{\partial q}{\partial t} = \left(-\nu \frac{\partial}{\partial x} + \gamma \frac{\partial^2}{\partial x^2} + \mu \right) q - a|q|^2 q, \quad x \in (-\infty, \infty), \quad q(x, t) \in \mathbb{C},$$

457 with parameters $a = 0.1$, $\gamma = 1 - i$, $\nu = 2 + 0.4i$ and $\mu = (\mu_0 - 0.2^2) + \mu_2 x^2 / 2$ with $\mu_2 = -0.01$
 458 and $\mu_0 = 0.38$. Here, $i = \sqrt{-1}$. For this choice of parameters, the origin $q(x, t) = 0$ is linearly
 459 stable, but exhibits significant transient growth due to the non-normal nature of the linear
 460 dynamics [17]. This type of behavior is common in high-shear flows (e.g., boundary layers,
 461 mixing layers and jets), making the CGL a meaningful and widely-used benchmark example.
 462 In this section, we are interested in computing ROMs capable of predicting the input-output
 463 dynamics of (4.1) in response to spatially-localized inputs. In particular, we wish to predict
 464 the time history of complex-valued measurements

$$465 \quad (4.2) \quad y = Cq = \exp \left\{ - \left(\frac{x + \bar{x}}{s} \right)^2 \right\} q$$

466 in response to complex-valued inputs u that enter the dynamics according to

$$467 \quad (4.3) \quad Bu = \exp \left\{ - \left(\frac{x - \bar{x}}{s} \right)^2 \right\} u.$$

468 Here, $s = 1.6$ and $\bar{x} = -\sqrt{-2(\mu_0 - 0.2^2)/\mu_2}$ is the location of the so-called “branch I” of the
 469 disturbance-amplification region (see [17] for additional details). Upon spatial discretization
 470 on a grid with n nodes, equation (4.1) can be written as a real-valued dynamical system with

471 cubic dynamics

$$472 \quad (4.4) \quad \begin{aligned} \frac{d\mathbf{q}}{dt} &= \mathbf{A}\mathbf{q} + \mathbf{H} : (\mathbf{q} \otimes \mathbf{q} \otimes \mathbf{q}) + \mathbf{B}\mathbf{u} \\ \mathbf{y} &= \mathbf{C}\mathbf{q}, \end{aligned}$$

473 where the state $\mathbf{q} \in \mathbb{R}^{2n}$ contains the spatially-discretized real and imaginary components
 474 of q , $\mathbf{u} \in \mathbb{R}^2$ contains the real and imaginary components of the input u and $\mathbf{y} \in \mathbb{R}^2$ contains
 475 the real and imaginary components of the output y . Thus, given the form of the full-order
 476 system, we seek cubic reduced-order models with dynamics expressed as the sum of a linear
 477 term, a cubic term and a linear input term.

478 We train our models by simulating the response of (4.4) to impulses

$$479 \quad (4.5) \quad \mathbf{B}\mathbf{u}(t) = \begin{cases} \beta \mathbf{B}\mathbf{e}_j & \text{if } t = 0 \\ 0 & \text{if } t \neq 0 \end{cases}$$

480 where $\mathbf{e}_j \in \mathbb{R}^2$ is the unit-norm vector in the standard basis and $\beta \in \{-1.0, 0.01, 0.1, 1.0\}$.
 481 We therefore have a total of $N_{\text{traj}} = 8$ training trajectories, and we collect the output \mathbf{y}
 482 at $N = 1000$ uniformly-spaced time instances $t_i \in [0, 1000]$. Since the leading five POD
 483 modes associated with the training data contain approximately 98% of the variance and are
 484 sufficient to reconstruct the time history of the output \mathbf{y} almost perfectly, we seek models of
 485 size $r = 5$. The cost functions for NiTROM, TrOOP and Operator Inference are analogous
 486 to those considered in section 3, except that the reduced-order dynamics are cubic and the
 487 normalization constants α_j in (3.7) are defined as the time-averaged energy of the output \mathbf{y}
 488 along the j th trajectory. In Operator Inference, the regularization parameter for the reduced-
 489 order fourth-order tensor was chosen as $\lambda = 10^9$ following the same criterion described in the
 490 previous section. The NiTROM optimization was initialized with $\Phi = \Psi$ given by the first
 491 five POD modes of the training data and the reduced-order tensors provided by Operator
 492 Inference. The optimization was conducted using *coordinate* descent by successively holding
 493 the reduced-order tensors fixed and allowing for the bases Φ and Ψ to vary, and viceversa. On
 494 this particular example, we found this procedure to be less prone to getting stuck in ‘‘bad’’
 495 local minima. TrOOP, on the other hand, was initialized with Φ and Ψ given by Balanced
 496 Truncation [22, 30] since the initialization with POD modes led to a rather inaccurate local
 497 minimum. TrOOP’s optimization was carried out using conjugate gradient.

498 We test the performance of our model by generating 50 trajectories in response to inputs
 499 of the form (4.5) with β drawn uniformly at random from $[-1.0, 1.0]$. The average error across
 500 all testing trajectories is shown in figure 4a, while a representative impulse response is shown
 501 in figure 4b. Overall, we see that both NiTROM and TrOOP achieve very good predictive
 502 accuracy and are capable of tracking the output through the heavy oscillatory transients. By
 503 contrast, Operator Inference and the POD-Galerkin model exhibit higher errors, and this is
 504 most likely due to the highly non-normal nature of the CGL dynamics. In fact, both these
 505 methods achieve dimensionality reduction by orthogonally projecting the state onto the span
 506 of POD modes, while, as previously discussed, reduced-order models for non-normal systems
 507 typically require carefully chosen oblique projections. Finally, we demonstrate the predictive
 508 accuracy of NiTROM on unseen sinusoidal inputs of the form $\mathbf{B}\mathbf{u}(t) = 0.05 \sin(k\omega t)\mathbf{B}\mathbf{v}/\|\mathbf{B}\mathbf{v}\|$,

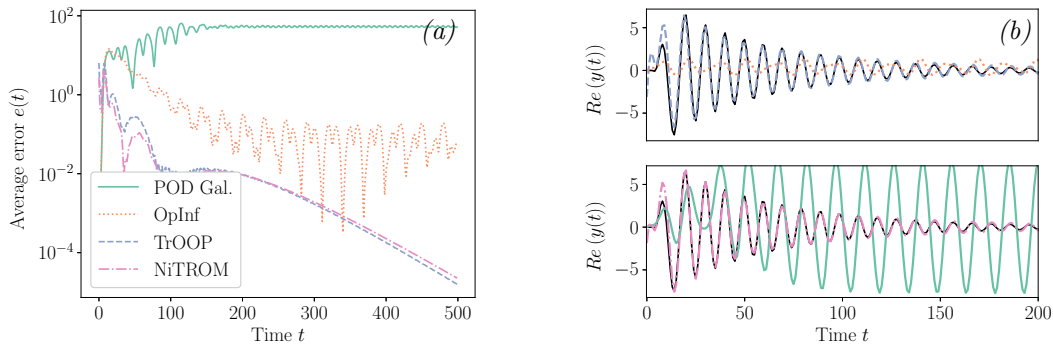


Figure 4: CGL: (a) average testing error (analogous to (3.9)). (b) Real part of the output y from a representative testing impulse response. The black line in panel (b) denotes the ground-truth response.

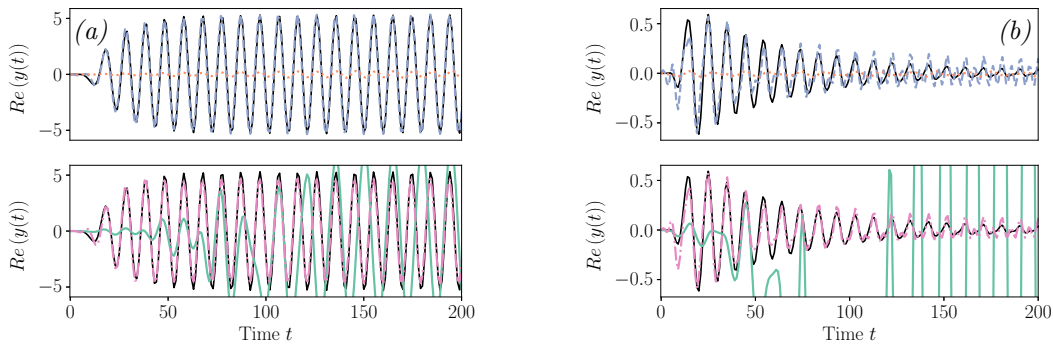


Figure 5: CGL: Real part of the output y in response to a sinusoidal input with frequencies (a) ω and (b) 2ω , where $\omega \approx 0.648$ is the fundamental frequency of the system. The black continuous line indicates the ground truth, and the rest of the legend is in figure 4a.

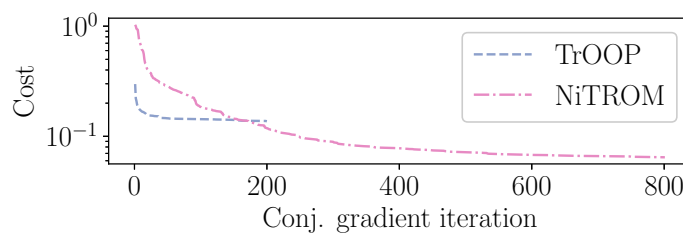


Figure 6: CGL: Cost function value versus conjugate gradient iteration for the CGL equation. TrOOP was initialized using Balanced Truncation, while NiTROM using Operator Inference.

509 where $\mathbf{v} \in \mathbb{R}^2$ is chosen at random and $\omega \approx 0.648$ is the natural frequency of the system. The
 510 results for frequencies ω and 2ω are shown in figure 5, where we see that NiTROM provides an
 511 accurate estimate of the response of the system at frequency ω and an acceptable prediction
 512 at frequency 2ω . The reason why the prediction at 2ω for both TrOOP and NiTROM is not
 513 as clean as the prediction at ω is because the training data exhibited dominant oscillatory
 514 dynamics at the natural frequency ω and very little contributions from other frequencies.
 515 Nonetheless, the predictions at 2ω are better than those provided by POD-Galerkin and
 516 Operator Inference. Before closing this example, we report on the loss function value for both
 517 TrOOP and NiTROM in figure 6, but we remark that TrOOP was initialized using Balanced
 518 Truncation, while NiTROM was initialized using Operator Inference.

519 **5. Application to the lid-driven cavity flow.** In this section, we apply our model reduction
 520 procedure to an incompressible fluid flow inside a lid-driven square cavity. The flow dynamics
 521 are governed by the incompressible Navier-Stokes equation and by the continuity equation

$$522 \quad (5.1) \quad \frac{\partial \mathbf{v}}{\partial t} + \mathbf{v} \cdot \nabla \mathbf{v} = -\nabla p + Re^{-1} \nabla^2 \mathbf{v}$$

$$523 \quad (5.2) \quad \nabla \cdot \mathbf{v} = 0,$$

524 where $\mathbf{v}(\mathbf{x}, t) = (u(\mathbf{x}, t), v(\mathbf{x}, t))$ is the two-dimensional velocity vector, $p(\mathbf{x}, t)$ is the pressure
 525 and Re is the Reynolds number. Throughout, we consider a two-dimensional spatial domain
 526 $D = [0, 1] \times [0, 1]$ with zero-velocity boundary conditions at all walls, except for $u = 1$ at the
 527 top wall. The Reynolds number is held at $Re = 8300$, where the flow admits a linearly stable
 528 steady state (shown in figure 7a), but exhibits large amplification and significant transient
 529 growth due to the non-normal nature of the underlying linear dynamics. The high degree of
 530 non-normality and consequent transient growth can be appreciated by looking at figure 7b,
 531 where we show the time history of the energy of several impulse responses. In particular, we
 532 see that after an initial decay, the energy spikes around $t = 5$ before decaying back to zero.
 533 We discretize the governing equations using a second-order finite-volume scheme on a uniform
 534 fully-staggered grid of size $N_x \times N_y = 100 \times 100$. With this spatial discretization, no pressure
 535 boundary conditions need to be imposed. The temporal integration is carried out using the
 536 second-order fractional step (projection) method introduced in [9]. Our solver was validated
 537 by reproducing some of the results in [16].

538 In this example, we are interested in computing data-driven reduced-order models capable
 539 of predicting the evolution of the flow in response to spatially-localized inputs that enter the
 540 x -momentum equation as

$$541 \quad (5.3) \quad B(x, y)w(t) = \exp \left\{ -5000 \left((x - x_c)^2 + (y - y_c)^2 \right) \right\} w(t),$$

542 with $x_c = y_c = 0.95$. Upon spatial discretization and removal of the pressure via projection
 543 onto the space of divergence-free vector fields, the dynamics are governed by

$$544 \quad (5.4) \quad \frac{d}{dt} \mathbf{q} = \mathbf{A} \mathbf{q} + \mathbf{H} : \mathbf{q} \mathbf{q}^\top + \mathbf{B} w,$$

545 where $\mathbf{q} \in \mathbb{R}^N$ is the spatially-discretized divergence-free velocity field (with $N = 2N_x N_y =$
 546 2×10^4), \mathbf{A} governs the linear dynamics, \mathbf{H} is a third-order tensor representative of the

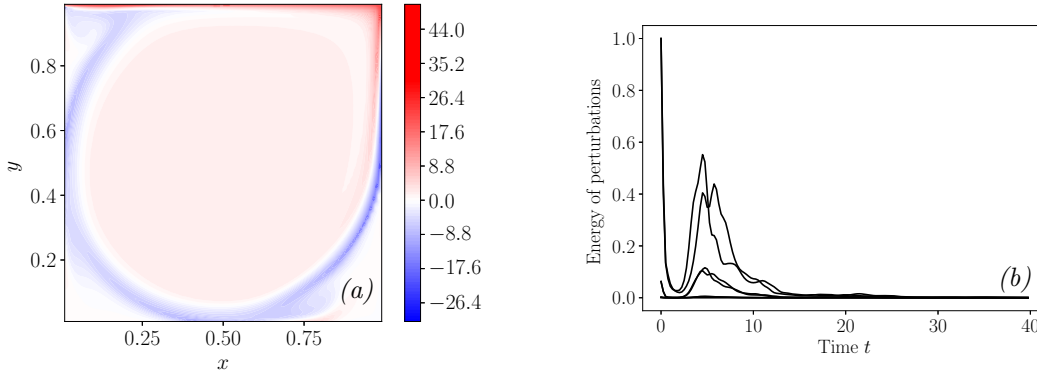


Figure 7: Cavity flow: panel (a) shows the vorticity field from the steady-state solution that exists at $Re = 8300$, and panel (b) shows the energy (i.e., the squared two norm) of the seven training trajectories.

547 quadratic nonlinearity in the Navier-Stokes equation and \mathbf{B} is the input matrix obtained
 548 from (5.3) after enforcing that \mathbf{B} generates a divergence-free vector. (For convenience, we also
 549 scale \mathbf{B} to unit norm.) Throughout the remainder of this section, we take $\mathbf{y} = \mathbf{q}$ (i.e., we
 550 observe the time evolution of the whole state).

551 **5.1. Training procedure.** We collect seven training trajectories by simulating (5.4) in
 552 response to impulses

$$553 \quad (5.5) \quad w(t) = \begin{cases} \beta & \text{if } t = 0 \\ 0 & \text{if } t \neq 0, \end{cases}$$

554 with $\beta \in \{-1.0, -0.25, -0.05, 0.01, 0.05, 0.25, 1.0\}$. The time history of the energy of the
 555 training trajectories is shown in figure 7b. We save 160 snapshots from each trajectory at
 556 equally-distributed temporal instances $t \in [0, 40]$, and then we perform POD. Using the first 50
 557 POD modes, which contain 99.6% of the variance in the training data, we compute an Operator
 558 Inference model by minimizing the cost function (2.29). We normalize the trajectories by their
 559 time-averaged energy and, as in the previous sections, we also penalize the Frobenius norm of
 560 the third-order tensor \mathbf{H} with the regularization parameter taken to be $\lambda = 10^{-3}$.

561 Given the complexity of the problem and the length of the trajectories, we train Ni-
 562 TROM as follows. First, we pre-project the data onto the span of the first 200 POD modes,
 563 which contain $> 99.99\%$ of the variance. This guarantees that the optimal NiTROM bases Φ
 564 and Ψ satisfy the divergence-free constraint in (5.2), since the POD modes are computed from
 565 divergence-free snapshots. Second, after initializing the search with the Operator Inference
 566 model, we train by progressively extending the length of the forecasting horizon. That is, we
 567 first optimize a model to make predictions up to $t = 2.5$, then $t = 5$, and so forth all the way
 568 up to $t = 40$.

569 Since, after a first pass, our model exhibited slightly unstable linear dynamics (possibly
 570 due to the presence of numerical noise and/or weak decaying oscillations in the tail end of the

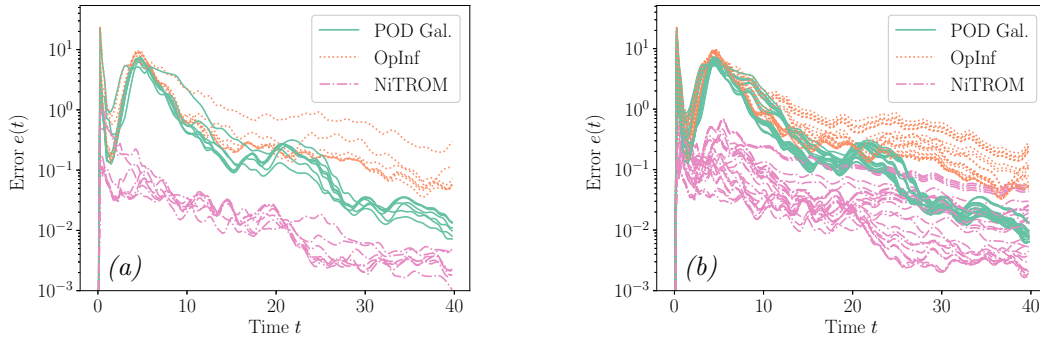


Figure 8: Cavity flow: panel (a) shows the training error from the 7 training impulse responses, and panel (b) shows the testing error computed for 25 unseen impulse responses. The error is defined in equation (5.8).

571 training data), we added a stability-promoting penalty to our cost function as follows,

572 (5.6)
$$\tilde{J} = J_{\text{NiTROM}} + \mu \|\hat{\mathbf{z}}_{\text{lin}}(t_f)\|^2.$$

573 Here, t_f is a sufficiently large time (chosen to be 100 in our case) and $\hat{\mathbf{z}}_{\text{lin}}$ satisfies

574 (5.7)
$$\frac{d\hat{\mathbf{z}}_{\text{lin}}}{dt} = \mathbf{A}_r \hat{\mathbf{z}}_{\text{lin}}, \quad \hat{\mathbf{z}}_{\text{lin}}(0) = \hat{\mathbf{z}}_{\text{lin},0},$$

575 with $\hat{\mathbf{z}}_{\text{lin},0}$ a unit-norm random vector. Notice that this penalty is truly stability-promoting, as
 576 it is analogous to penalizing the Frobenius norm of $e^{\mathbf{A}_r t_f}$, and shrinking the Frobenius norm
 577 of the exponential map corresponds to pushing the eigenvalues of \mathbf{A}_r farther into the left-half
 578 plane. The gradient of the penalty term with respect to \mathbf{A}_r can be computed straightforwardly
 579 following the same logic used in Proposition 2.1. The regularization parameter μ was held
 580 at zero for most of the training, until we reached a forecasting horizon $t = 40$ when we set
 581 $\mu = 10^{-3}$. The training was conducted using coordinate descent as described in section 4, and
 582 we stopped the optimization after approximately 2000 iterations.

583 **5.2. Testing.** In this section we compare NiTROM against Operator Inference and POD
 584 Galerkin. We do not compare against TrOOP because of its intrusive need to access the
 585 linearized dynamics and the adjoint, and because we are ultimately interested in comparing
 586 our formulation against other non-intrusive (or weakly intrusive) model reduction techniques.
 587 We test the models by generating 25 impulse responses with the impulse magnitude β drawn
 588 uniformly at random from $[-1, 1]$. The training and testing errors for NiTROM, Operator
 589 Inference and for the POD-Galerkin model (all with dimension $r = 50$) are shown in figure 8.
 590 The error is defined as

591 (5.8)
$$e(t) = \frac{N}{\sum_{i=0}^{N-1} \|\mathbf{q}(t)\|^2} \|\mathbf{q}(t) - \hat{\mathbf{q}}(t)\|^2,$$

592 where \mathbf{q} is the ground-truth and $\hat{\mathbf{q}}$ is the prediction given by the reduced-order model. From
 593 the figure, we see that NiTROM maintains a low error across all trajectories and for all times.

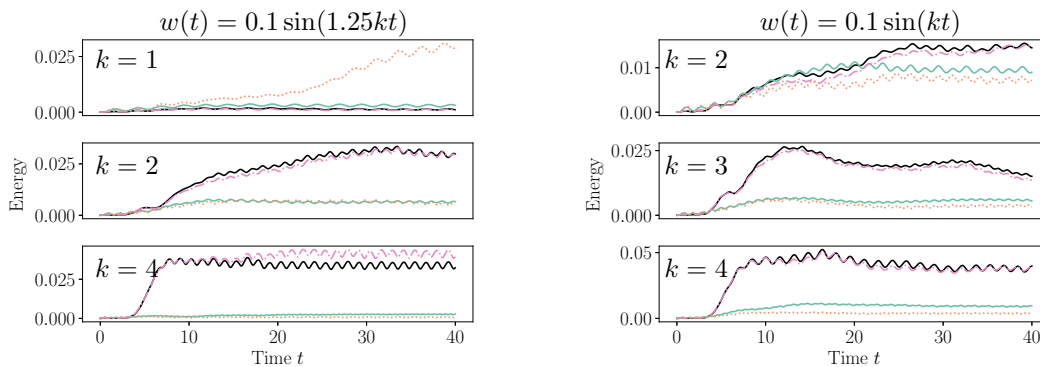


Figure 9: Cavity flow: evolution of the energy of the perturbations in response to sinusoidal inputs $w(t)$. The black line is the full-order model and the rest of the legend is in figure 8.

594 In particular, we observe that around $t = 5$ (when the fluid exhibits its peak in transient
 595 growth, as illustrated in figure 7b) the errors produced by POD Galerkin and Operator Infer-
 596 ence can be one to two orders of magnitude larger than those produced by NiTROM.

597 As in the previous section, we also test the ability of our reduced-order model to predict
 598 the response of the fluid to sinusoidal inputs $w(t) = 0.1 \sin(k\omega t)$ starting from the stable
 599 steady state. The results are shown in figure 9, where we see the response to harmonics of
 600 $\omega = 1.25$ and $\omega = 1$, which are frequencies that are naturally excited by the linear dynamics
 601 of the flow. In all cases, NiTROM exhibits better predictive accuracy than the other models,
 602 and it is capable of tracking the early-stage sharp growth of the perturbations as well as
 603 the cavity's long-time oscillatory behavior. Finally, in order to gain further insight into the
 604 performance of these models, we show vorticity snapshots at time $t = 35$ from two of the
 605 trajectories with frequency. In figure 10, where the forcing frequency was 4.00, Operator
 606 Inference and POD Galerkin underestimate the magnitude of the vorticity and they predict
 607 the wrong phase of the vortical structures (observe the vorticity field near the bottom wall at
 608 $x = 0.5$). In figure 11, where the forcing frequency is 1.25, on the other hand, POD Galerkin
 609 provides a reasonable approximation of the vortical structures despite slightly overestimating
 610 the vorticity magnitude, while the Operator Inference estimate is overall quite far from the
 611 ground truth. By contrast, NiTROM provides an accurate estimate of the vorticity phase and
 612 magnitude in both cases.

613 **6. Conclusion.** In this paper, we have introduced a novel non-intrusive data-driven frame-
 614 work to compute accurate reduced-order models of high-dimensional systems that exhibit
 615 large-amplitude transient growth. These systems are ubiquitous in fluid mechanics, and they
 616 are known to pose challenges to model reduction methods that achieve dimensionality reduc-
 617 tion via orthogonal projection onto a low-dimensional subspace (or, more generally, onto a
 618 low-dimensional nonlinear manifold). While these challenges can be addressed by intrusive
 619 methods that leverage the underlying form of the governing equations to compute an ap-
 620 propriate oblique projection, purely data-driven frameworks tend to achieve dimensionality
 621 reduction via orthogonal projection and this can lead to models with poor predictive accuracy.

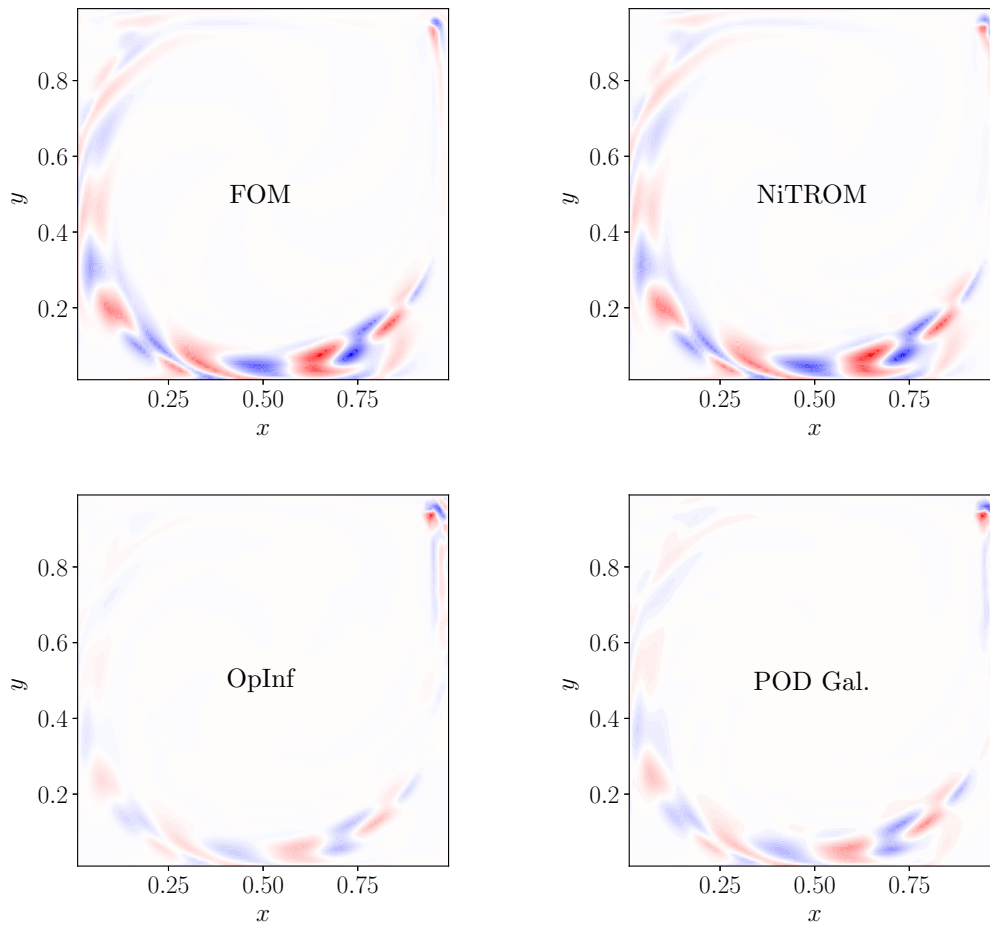


Figure 10: Cavity flow: vorticity field at time $t = 35$ from the trajectory with forcing frequency 4.00 in figure 9. Red indicates positive vorticity with maximum value 0.73, blue indicates negative vorticity with minimum value -0.73 and white is zero vorticity.

622 Given trajectories from the full-order system, we address this issue by solving an optimization
 623 problem to simultaneously find optimal oblique projection operators and reduced-order dy-
 624 namics on their range. The framework is termed NiTROM—“Non-intrusive Trajectory-based
 625 optimization of Reduced-Order Models”—and it is demonstrated on three examples: a simple
 626 toy model governed by three ordinary differential equations, the complex Ginzburg-Landau
 627 equations and a two-dimensional incompressible lid-driven cavity flow at Reynolds number
 628 $Re = 8300$. In all these examples, NiTROM outperforms state-of-the-art non-intrusive and
 629 weakly-intrusive methods that rely on orthogonal projections for dimension reduction, and, in
 630 the first two examples it exhibits similar performance to optimal (intrusive) Petrov-Galerkin
 631 reduced-order models obtained using the recently-introduced TrOOP formulation [25]. Cur-
 632 rently, NiTROM is formulated as a linear projection model reduction method, but, in the

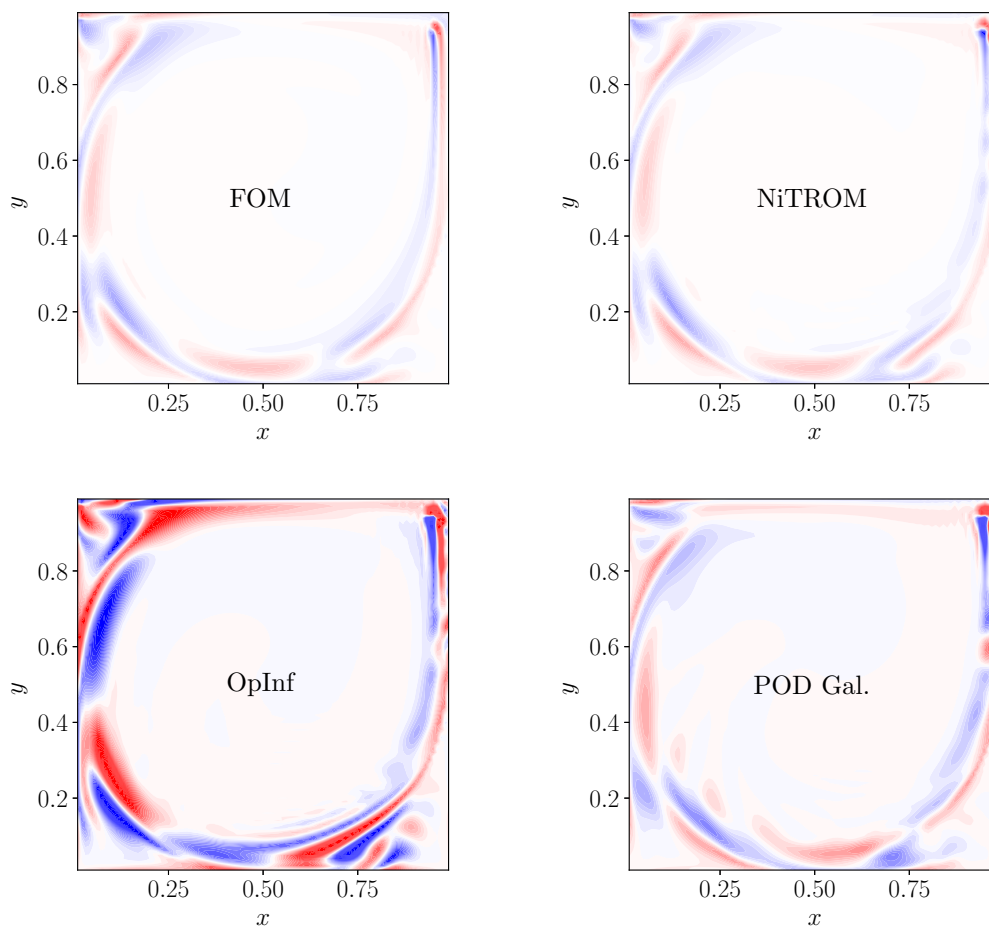


Figure 11: Cavity flow: vorticity field at time $t = 35$ from the trajectory with forcing frequency 1.25 in figure 9. Red indicates positive vorticity with maximum value 0.18, blue indicates negative vorticity with minimum value -0.18 and white is zero vorticity.

633 future, it would be interesting to explore the possibility of extending it to quadratic (and,
 634 more generally, polynomial) manifolds, as done within the Operator Inference formulation
 635 in [14].

636 **Acknowledgments.** This material is based upon work supported by the National Sci-
 637 ence Foundation under Grant No. 2139536, issued to the University of Illinois at Urbana-
 638 Champaign by the Texas Advanced Computing Center under subaward UTAUS-SUB00000545
 639 with Dr. Daniel Stanzione as the PI.

640

REFERENCES

- 641 [1] P.-A. ABSIL, R. MAHONY, AND R. SEPULCHRE, *Optimization algorithms on matrix manifolds*, Princeton
642 University Press, 2009.
- 643 [2] M. F. BARONE, I. KALASHNIKOVA, D. J. SEGALMAN, AND H. K. THORNQUIST, *Stable galerkin reduced*
644 *order models for linearized compressible flow*, *Journal of Computational Physics*, 228 (2009), pp. 1932–
645 1946.
- 646 [3] P. BENNER AND T. BREITEN, *Interpolation-based H_2 -model reduction of bilinear control systems*, *SIAM*
647 *Journal on Matrix Analysis and Applications*, 33 (2012), pp. 859–885.
- 648 [4] P. BENNER AND P. GOYAL, *Balanced truncation model order reduction for quadratic-bilinear control*
649 *systems*, arXiv preprint arXiv:1705.00160, (2017).
- 650 [5] P. BENNER, P. GOYAL, AND S. GUGERCIN, *H_2 -quasi-optimal model order reduction for quadratic-bilinear*
651 *control systems*, *SIAM Journal on Matrix Analysis and Applications*, 39 (2018), pp. 983–1032.
- 652 [6] P. BENNER, P. GOYAL, J. HEILAND, AND I. PONTES DUFF, *A quadratic decoder approach to nonintrusive*
653 *reduced-order modeling of nonlinear dynamical systems*, *PAMM*, 23 (2023), p. e202200049.
- 654 [7] N. BOUMAL, B. MISHRA, P.-A. ABSIL, AND R. SEPULCHRE, *Manopt, a matlab toolbox for optimization*
655 *on manifolds*, *Journal of Machine Learning Research*, 15 (2014), pp. 1455–1459.
- 656 [8] J.-M. CHOMAZ, *Global instabilities in spatially-developing flows: Non-normality and nonlinearity*, *Annual*
657 *Review of Fluid Mechanics*, 37 (2005), pp. 357–392.
- 658 [9] A. J. CHORIN, *Numerical solution of the Navier-Stokes equations*, *Mathematics of Computation*, 22
659 (1968), pp. 745–762.
- 660 [10] P. CONTI, G. GOBAT, S. FRESCA, A. MANZONI, AND A. FRANGI, *Reduced order modeling of parametrized*
661 *systems through autoencoders and sindy approach: continuation of periodic solutions*, *Computer Meth-*
662 *ods in Applied Mechanics and Engineering*, 411 (2023), p. 116072.
- 663 [11] G. E. DULLERUD AND F. PAGANINI, *A Course in Robust Control Theory: a Convex Approach*, Springer
664 New York, 2000.
- 665 [12] G. FLAGG, C. A. BEATTIE, AND S. GUGERCIN, *Interpolatory H_∞ model reduction*, *Systems & Control*
666 *Letters*, 62 (2013).
- 667 [13] S. FRESCA, L. DEDE', AND A. MANZONI, *A comprehensive deep learning-based approach to reduced order*
668 *modeling of nonlinear time-dependent parametrized PDEs*, *Journal of Scientific Computing*, 87 (2021),
669 p. 61.
- 670 [14] R. GEELLEN, S. WRIGHT, AND K. WILLCOX, *Operator inference for non-intrusive model reduction*
671 *with quadratic manifolds*, *Computer Methods in Applied Mechanics and Engineering*, 403 (2023),
672 p. 115717.
- 673 [15] Y. GENG, J. SINGH, L. JU, B. KRAMER, AND Z. WANG, *Gradient preserving operator inference: Data-*
674 *driven reduced-order models for equations with gradient structure*, *Computer Methods in Applied*
675 *Mechanics and Engineering*, 427 (2024), p. 117033.
- 676 [16] U. GHIA, K. GHIA, AND C. SHIN, *High-Re solutions for incompressible flow using the Navier-Stokes*
677 *equations and a multigrid method*, *Journal of Computational Physics*, 48 (1982), pp. 387–411.
- 678 [17] M. ILAK, S. BAGHERI, L. BRANDT, C. W. ROWLEY, AND D. S. HENNINGSON, *Model reduction of*
679 *the nonlinear complex Ginzburg–Landau equation*, *SIAM Journal on Applied Dynamical Systems*, 9
680 (2010), pp. 1284–1302.
- 681 [18] O. ISSAN AND B. KRAMER, *Predicting solar wind streams from the inner-heliosphere to earth via shifted*
682 *operator inference*, *Journal of Computational Physics*, 473 (2023).
- 683 [19] B. KRAMER, B. PEHERSTORFER, AND K. E. WILLCOX, *Learning nonlinear reduced models from data*
684 *with operator inference*, *Annual Review of Fluid Mechanics*, 56 (2024).
- 685 [20] Z. MA, C. W. ROWLEY, AND G. TADMOR, *Snapshot-based balanced truncation for linear time-periodic*
686 *systems*, *IEEE Transactions on Automatic Control*, 55 (2010), pp. 469–473.
- 687 [21] S. A. MCQUARRIE, C. HUANG, AND K. E. WILLCOX, *Data-driven reduced-order models via regularised*
688 *operator inference for a single-injector combustion process*, *Journal of the Royal Society of New*
689 *Zealand*, 51 (2021), pp. 194–211.
- 690 [22] B. MOORE, *Principal component analysis in linear systems: Controllability, observability, and model*
691 *reduction*, *IEEE Transactions on Automatic Control*, 26 (1981), pp. 17–32.
- 692 [23] B. R. NOACK, K. AFANASIEV, M. MORZYŃSKI, G. TADMOR, AND F. THIELE, *A hierarchy of low-*
693 *dimensional models for the transient and post-transient cylinder wake*, *Journal of Fluid Mechanics*,
694 497 (2003), pp. 335–363.

- 695 [24] S. E. OTTO, G. R. MACCHIO, AND C. W. ROWLEY, *Learning nonlinear projections for reduced-order*
696 *modeling of dynamical systems using constrained autoencoders*, *Chaos: An Interdisciplinary Journal*
697 *of Nonlinear Science*, 33 (2023), p. 113130.
- 698 [25] S. E. OTTO, A. PADOVAN, AND C. W. ROWLEY, *Optimizing oblique projections for nonlinear systems*
699 *using trajectories*, *SIAM Journal on Scientific Computing*, 44 (2022), pp. A1681–A1702.
- 700 [26] S. E. OTTO, A. PADOVAN, AND C. W. ROWLEY, *Model reduction for nonlinear systems by balanced trun-*
701 *cation of state and gradient covariance*, *SIAM Journal on Scientific Computing*, 45 (2023), pp. A2325–
702 A2355.
- 703 [27] A. PADOVAN AND C. W. ROWLEY, *Continuous-time balanced truncation for time-periodic fluid flows*
704 *using frequential Gramians*, *Journal of Computational Physics*, 496 (2024), p. 112597.
- 705 [28] B. PEHERSTORFER AND K. WILLCOX, *Data-driven operator inference for nonintrusive projection-based*
706 *model reduction*, *Computer Methods in Applied Mechanics and Engineering*, 306 (2016), pp. 196–215.
- 707 [29] E. QIAN, I.-G. FARCAŞ, AND K. WILLCOX, *Reduced operator inference for nonlinear partial differential*
708 *equations*, *SIAM Journal on Scientific Computing*, 44 (2022), pp. A1934–A1959.
- 709 [30] C. W. ROWLEY, *Model reduction for fluids using balanced proper orthogonal decomposition*, *Int. J. of*
710 *Bifurcation and Chaos*, 15 (2005), pp. 997–1013.
- 711 [31] C. W. ROWLEY, T. COLONIUS, AND R. M. MURRAY, *Model reduction for compressible flows using POD*
712 *and Galerkin projection*, *Physica D: Nonlinear Phenomena*, 189 (2004), pp. 115–129.
- 713 [32] C. W. ROWLEY AND S. T. M. DAWSON, *Model reduction for flow analysis and control*, *Annual Review*
714 *of Fluid Mechanics*, 49 (2017), pp. 387–417.
- 715 [33] P. SASHITTAL AND D. J. BODONY, *Reduced-order control using low-rank dynamic mode decomposition*,
716 *Theoretical and Computational Fluid Dynamics*, 33 (2019), p. 603–623.
- 717 [34] N. SAWANT, B. KRAMER, AND B. PEHERSTORFER, *Physics-informed regularization and structure preser-*
718 *vation for learning stable reduced models from data with operator inference*, *Computer Methods in*
719 *Applied Mechanics and Engineering*, 404 (2023), p. 115836.
- 720 [35] H. SHARMA, Z. WANG, AND B. KRAMER, *Hamiltonian operator inference: Physics-preserving learning*
721 *of reduced-order models for canonical hamiltonian systems*, *Physica D: Nonlinear Phenomena*, 431
722 (2022), p. 133122.
- 723 [36] J. TOWNSEND, N. KOEP, AND S. WEICHWALD, *Pymanopt: A Python toolbox for optimization on mani-*
724 *folds using automatic differentiation*, *Journal of Machine Learning Research*, 17 (2016), p. 1–5.
- 725 [37] P. VAN DOOREN, K. GALLIVAN, AND P.-A. ABSIL, *\mathcal{H}_2 -optimal model reduction of mimo systems*, *Applied*
726 *Mathematics Letters*, 21 (2008), pp. 1267–1273.
- 727 [38] A. VARGA, *Balanced truncation model reduction of periodic systems*, in *Proceedings of the 39th IEEE*
728 *Conference on Decision and Control*, vol. 3, 2000, pp. 2379–2384.
- 729 [39] K. WILLCOX AND J. PERAIRE, *Balanced model reduction via the proper orthogonal decomposition*, *AIAA*
730 *Journal*, 40 (2002), pp. 2323–2330.